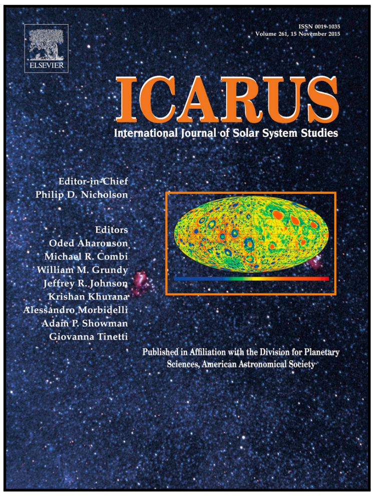

Solar Energetic Particles (SEP) and Galactic Cosmic Rays (GCR) as tracers of solar wind conditions near Saturn: event lists and applications

E. Roussos, C.M. Jackman, M.F. Thomsen, W.S. Kurth, S.V. Badman, C. Paranicas, P. Kollmann, N. Krupp, R. Bučík, D.G. Mitchell, S.M. Krimigis, D.C. Hamilton, A. Radioti

PII: S0019-1035(17)30361-5
DOI: 10.1016/j.icarus.2017.08.040
Reference: YICAR 12595

To appear in: *Icarus*

Received date: 12 May 2017
Revised date: 2 August 2017
Accepted date: 30 August 2017

Highlights

- Energetic particles used for non-stop monitoring of solar wind transients at Saturn
- 63 intervals of CME and CIRs impacting Saturn identified between 2004 and 2016
- Solar-wind induced dynamics in Saturns electron radiation belts are now resolved
- A strong magnetospheric compression at Saturn has also been linked to a CME event
- Numerous options to study Saturns magnetospheric response to the solar wind

Solar Energetic Particles (SEP) and Galactic Cosmic Rays (GCR) as tracers of solar wind conditions near Saturn: event lists and applications

E. Roussos (roussos@mps.mpg.de)[a], C. M. Jackman[b], M. F. Thomsen[c], W.S. Kurth[d], S. V. Badman[e], C. Paranicas[f], P. Kollmann[f], N. Krupp[a], R. Bučík[a,g], D.G. Mitchell[f], S. M. Krimigis[f,j], D.C. Hamilton[h], A. Radioti[i]

[a]*Max Planck Institute for Solar System Research, Justus-von-Liebig-Weg 3, 37077, Göttingen, Germany*
[b]*School of Physics and Astronomy, University of Southampton, Southampton, United Kingdom*
[c]*Planetary Science Institute, 85719, USA*
[d]*Department of Physics and Astronomy, University of Iowa, Iowa City, Iowa, USA*
[e]*Physics Department, Lancaster University, Lancaster, UK*
[f]*Johns Hopkins University Applied Physics Laboratory, 11100 Johns Hopkins Road, Laurel, MD 20723-6099, USA*
[g]*Institute für Astrophysik, Georg-August-Universität Göttingen, D-37077, Gttingen, Germany*
[h]*University of Maryland, College Park, MD 20742, USA*
[i]*Laboratoire de Physique Atmospherique et Planetaire- Université de Liége*
[j]*Office of Space Research and Technology, Academy of Athens , Greece*

Abstract

The lack of an upstream solar wind monitor poses a major challenge to any study that investigates the influence of the solar wind on the configuration and the dynamics of Saturn's magnetosphere. Here we show how Cassini MIMI/LEMMS observations of Solar Energetic Particle (SEP) and Galactic Cosmic Ray (GCR) transients, that are both linked to energetic processes in the heliosphere such us Interplanetary Coronal Mass Ejections (ICMEs) and Corotating Interaction Regions (CIRs), can be used to trace enhanced solar wind conditions at Saturn's distance. SEP protons can be easily distinguished from magnetospheric ions, particularly at the MeV energy range. Many SEPs are also accompanied by strong GCR Forbush Decreases. GCRs are detectable as a low count-rate noise signal in a large number of LEMMS channels. As SEPs and GCRs can easily penetrate into the outer and middle magnetosphere, they can be monitored continuously, even when Cassini is not situated in the solar wind. A survey of the MIMI/LEMMS dataset between 2004 and 2016 resulted in the identification of 46 SEP events. Most events last more than two weeks and have their lowest occurrence rate around the extended solar minimum between 2008 and 2010, suggesting that they are associated to ICMEs rather than CIRs, which are the main source of activity during the declining phase and the minimum of the solar cycle. We also list of 17 time periods (> 50 days each) where GCRs show a clear solar periodicity ($\sim$13 or 26 days). The 13-day period that derives from two CIRs per solar rotation dominates over the 26-day period in only one of the 17 cases catalogued. This interval belongs to the second half of 2008 when expansions of Saturn's electron radiation belts were previously reported to show a similar periodicity. That observation not only links the variability of Saturn's electron belts to solar wind processes, but also indicates that the source of the observed periodicity in GCRs may be local. In this case GCR measurements can be used to provide the phase of CIRs at Saturn. We further demonstrate the utility of our survey results by determining that: (a) Magnetospheric convection induced by solar wind disturbances associated with SEPs is a necessary driver for the formation of transient radiation belts that were observed throughout Saturn's magnetosphere on several occasions during 2005 and on day 105 of 2012. (b) An enhanced solar wind perturbation period that is connected to an SEP of day 332/2013 was the definite source of a strong magnetospheric compression which led to open flux loading in the magnetotail. Finally, we propose how the event lists can define the basis for single case studies or statistical investigations on how Saturn and its moons (particularly Titan) respond to extreme solar wind conditions or on the transport of SEPs and GCRs in the heliosphere.

Keywords: Saturn; Magnetosphere, Solar Energetic Particles, Galactic Cosmic Rays, Radiation belts

---

1. Introduction

Saturn is a rapidly rotating planet with a strong magnetic field that contains a strong plasma source (Enceladus) within its magnetospheric boundaries (Dougherty et al., 2006). It is because of these characteristics that the configuration and dynamics of the planet's magnetosphere is largely controlled by internal processes such as mass loading and outward radial transport of heavy ion plasma. Many observations are consistent with this picture, see for instance the reviews by Blanc et al. (2015) and Delamere et al. (2015). Whether the solar wind is an important or a secondary driver of magnetospheric dynamics cannot be easily assessed, primarily due to the lack of a dedicated monitor of the upstream solar wind conditions.

The influence of the solar wind on the structure and dynamics of Saturn's magnetosphere has been the subject of many investigations. Imaging of the aurora while Cassini monitors the solar wind is a technique that has been used frequently in order to infer the planet's magnetospheric responses (Prangé et al., 2004; Crary et al., 2005) but that method offers only indirect information regarding the charged particle distributions and the magnetic field configuration within the magnetosphere. Carbary et al. (2013), Carbary and Rymer (2017) and Roussos et al. (2014) identified solar periodicities in statistical analyses of energetic ion and electron measurements at Saturn but could not determine the exact physical process behind those findings. Finally, the use of models that predict the solar wind conditions at the two planets offers another option to link the upstream enviroment with in-situ or remote observations of the magnetospheres (Jackman et al., 2010; Provan et al., 2015). Correlation studies between measured and model-derived solar wind parameters, on the other hand, reveal time offsets for the onset of single-case events (e.g. in shock arrival times) that may vary between 10 hours and several days (Tao et al., 2005; Zieger and Hansen, 2008; Witasse et al., 2017).

An alternative proxy of the conditions upstream of Saturn's magnetosphere is offered through the detection of Solar Energetic Particles (SEPs) and Galactic Cosmic Rays (GCRs). SEP events involve enhanced fluxes of suprathermal protons, heavier ions and electrons, but unless otherwise stated, here we will always refer to their MeV proton component. SEPs can be accelerated directly in the flares, by Coronal Mass Ejection (CME) driven shocks in the corona or the interplanetary counterpart of CMEs, ICMEs. Another population of energetic particles can be accelerated by CIRs in interplanetary space (Cane et al., 1988; Reames, 1999). GCRs are mainly protons with energies above about several hundred MeV to 1 GeV, where they dominate over SEPs (also called Solar Cosmic Rays). They are accelerated at astrophysical sources and fill the heliosphere. Besides their long term modulation by the 11-year solar cycle, GCRs feature also short term changes which can be episodic or periodic. The most common episodic variations of GCRs are the so-called Forbush Decreases (FD) (Lockwood, 1971). FDs are fast decreases of the GCR intensity followed by a slower exponential recovery that at Earth may last up to about a week. They are caused by enhanced magnetic fields in the heliopshere that deflect GCRs. GCR variations at the solar rotation period (or its harmonics) have been attributed to CIRs (Barnes and Simpson, 1976; Simpson, 1998), while FDs to ICMEs and their associated shocks (Cane, 2000). It is therefore clear that measurements of SEPs and GCRs can provide clues for periods of perturbed solar wind upstream of Saturn.

An additional and very important advantage for using SEPs and GCRs as solar wind proxy is that the respective particles can directly access Saturn's outer and middle magnetosphere. The weakening of the dipolar field due to the current sheet configuration in Saturn's magnetosphere enhances this access. Kotova (2016) estimated that only 5-10% of 100 MeV protons would directly penetrate at 14 R_S if the configuration of Saturn's magnetosphere was purely dipolar (R_S is a Saturn radius, equal to 60268 km). This percentage is between 50-60% when a more realistic magnetic field model is used for similar calculations. For a comparison, Selesnick (2002) calculated that 50% of 100 MeV protons can directly reach into a distance of 30 R_J from Jupiter whereas in a dipole that distance would have been 70 R_J (1 R_J corresponds to one Jupiter radius). Lower energy SEPs (few MeV) cannot directly access low L-shells, but still can easily penetrate the magnetopause boundary. Observations indicate that they can fill Saturn's magnetosphere rapidly down to L$\sim$10 (where L is the dipole L-shell): Roussos et al. (2008, 2011) show $\sim$3 MeV proton SEP profiles developing uninterrupted as Cassini crosses into Saturn's middle magnetosphere. As a consequence, detecting SEPs and GCRs does not require the presence of a spacecraft in the solar wind. A spacecraft may have the opportunity to make in-situ particles and fields measurements within the magnetosphere of Saturn and simultaneously monitor a developing solar wind transient through SEPs and GCRs.

Several studies with Cassini have demonstrated how such observations can be used to study the influence of the upstream solar wind conditions on Saturn's magnetosphere, although the response of the magnetosphere was not always obvious. Roussos et al. (2008) identified three strong SEP events as the definite source of transient, MeV proton radiation belts that appeared approximatelly between the L-shell (L) of Tethys L$\sim$10. These SEP events were also accompanied by long duration FDs (Roussos et al., 2011). Simon et al. (2011) argued that these transient belts were the source of enhanced surface sputtering that gave rise to a tenuous exosphere at Saturn's moon Dione, although later studies have put this interpretation into question (Teolis and Waite, 2016). Roussos et al. (2014) investigated the impact of several large SEPs on the extension of the electron radiation belts and found an occasional correspondence. Provan et al. (2015) found that when Roussos et al. (2014) observed a cluster of SEP signatures around 2011, the predicted solar wind properties where consistent with extended periods of enhanced solar wind dynamic pressure, possibly explaining abrupt changes in the phase of Planetary Period Oscillations. Carbary et al. (2015) investigated whether the hinge of Saturn's magnetotail shows any abrupt changes during the occurrence of SEPs in 2013 and 2014 but could not resolve any obvious connection.

As no detailed list of SEP/GCR transients is available for the Cassini mission up to this date, in this study we review about 11 years of energetic particle observations by the MIMI/LEMMS detector (Krimigis et al., 2004) and identify 46 SEP events and 17 intervals of periodic GCR variations that could provide context for comprehensive investigations of the saturnian magnetosphere's response to the solar wind. After an extended introduction on specific aspects of SEPs, GCRs and their link to solar wind conditions at Saturn's distance (Section 2), we present the event lists together with the methodology used for the identification and the analysis of these transients (Sections 3-5). We conclude with Section 6, where we present two applications that demonstrate how the event lists can be used to understand aspects of the Saturn's magnetospheric dynamics.

2. Expectations for SEP and GCR transients at Saturn

Here we provide basic information regarding SEP and GCR transients in order to define a basis for understanding and interpreting Cassini measurements that we presented in the follow-up sections. The information provided is not exhaustive and for more details we refer the reader to the various studies cited in this section.

2.1. Observations at 1 AU

As discussed in the introduction, SEPs may originate from CMEs (and their interplanetary counterparts, ICMEs), CIRs and their associated shocks. SEPs associated to ICMEs will have an intensity profile that largely depends on the ICME observational geometry. For instance, the highest SEP intensities indicate the observer's magnetic connection to the nose of the interplanetary shock (where acceleration is the strongest) which is sometimes followed by a direct crossing of the ICME (or "ejecta"). The connection with the shock through the Interplanetary Magnetic Field (IMF) may be distant such that a time lag between an SEP event's onset/peak and the actual shock crossing

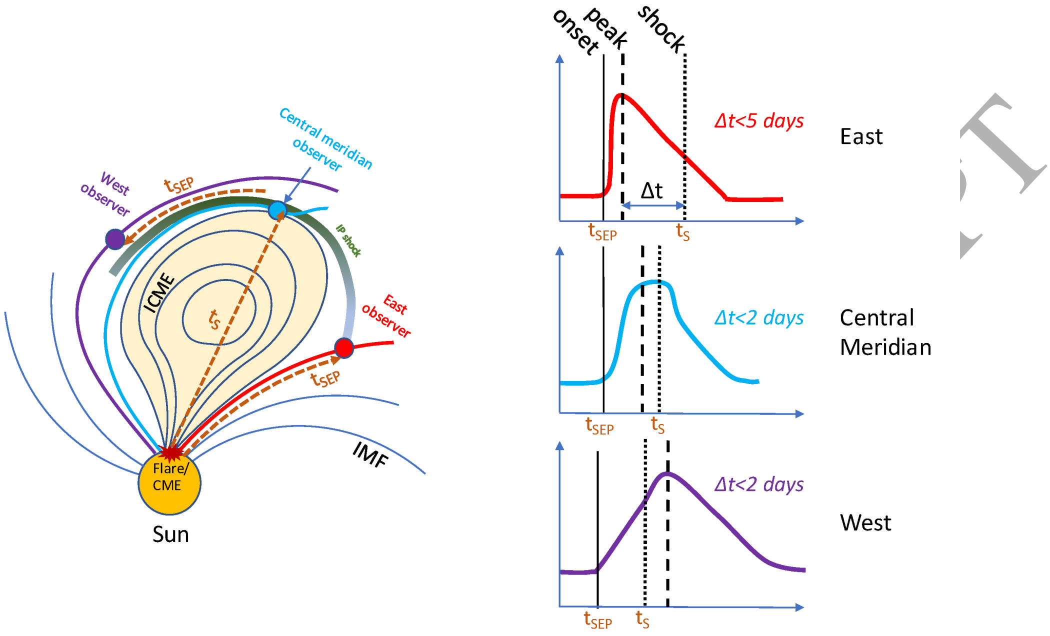

Figure 1: SEP profiles for different observer geometries with respect to a propagating ICME and its shock. The schematic is based on Reames (1999) and Cane et al. (1988) from observations in the inner heliosphere. The dotted vertical line indicates when the ICME shock passes the observer. The relevance for SEP observations at Saturn is discussed in the main text.

is usually present. The sketch of Figure 1, which derives from Reames (1999) and Cane et al. (1988), provides useful insights on the different ways SEPs may reach an observer, despite being based on observations at 1 AU.

An observer at east longitudes can get an early magnetic connection to the nose of shock leading the ICME, where SEP acceleration is the strongest. Since the time required for SEPs to travel from the shock to the observer along the IMF (t_{SEP}) is significantly shorter than the time the shock needs to reach the same location (t_S), the event's onset and peak will occur much earlier than the shock crossing. This time delay ($\Delta\, t$) can be up to about 5 days at 1 AU (Cane et al., 1988). The SEP intensity peaks impulsively soon after the onset since connection to the shock region has a short duration and/or because the observer gets gradually connected to weaker parts of the shock. The observer will also see that SEP intensity profiles are velocity (or energy)-time dispersed, with higher energy protons arriving faster.

Central meridian observers have a long duration connection to the interplanetary shock. A plateau in SEP intensity is formed, since the shock becomes weaker with time, while on the other hand the observer gets gradually connected magnetically to stronger parts of the shock. Energy-time dispersion is weaker compared to that seen by eastern observers. When the observer crosses into the ICME (or the "ejecta") behind the shock, a relatively sharp drop is observed in the MeV ion intensities. At 1 AU, Δt is less than two days. In addition, central meridian crossings are accompanied by two-step Forbush decreases (FDs). The first step is driven by the interplanetary shock while the second corresponds to the crossing into the strong magnetic field compression region of the ejecta (Cane, 2000; Arunbabu et al., 2013).

Observers at west longitudes will detect the SEP intensity peak after the IMF line they reside on is intercepted by the ICME and its shock at $t = t_S$. In that case, SEPs will be observed at $t = t_S + t_{SEP}$ and Δt will be small since $t_S \gg t_{SEP}$. Whether energy-time dispersed SEPs are observed will depend on the IMF line length from the shock to the observer. Both east and west observers may observe an FD, which may however have a single step since shocks are more extended longitudinally and are more likely to be sampled than the ejecta.

CIR-originating SEPs have several unique characteristics. For instance, CIR ion spectra may extend up to energies of about 20 MeV/n, while ICME shocks can accelerate ions to hundreds of MeV/n. Energy-time dispersion is weak and inversed: low energy particles tend to arrive first because CIR shocks become stronger with increasing heliocentric distance (Reames, 1999). FDs from CIRs are subtle and recur at the solar rotation period (Simpson, 1998).

2.2. Observations and expectations at 10 AU

At the heliocentric distance of Saturn and up to about 15 AU, ICMEs expand in longitude and the intensity of the interplanetary shock typically decreases. The expansion, however, may lead to the coalescence of different ICMEs, especially during the solar maximum (Prise et al., 2015). These form the (Global) Merged Interaction Regions (MIR or GMIR) that may drive strong shocks and high SEP ion fluxes (Wang and Richardson, 2002).

This merging may result in much more complex SEP profiles than the ones of the sketch of Figure 1 (e.g. multiple peaks). Also, as the Parker spiral wounds up at least once by 10 AU, IMF is nearly azimuthal in direction

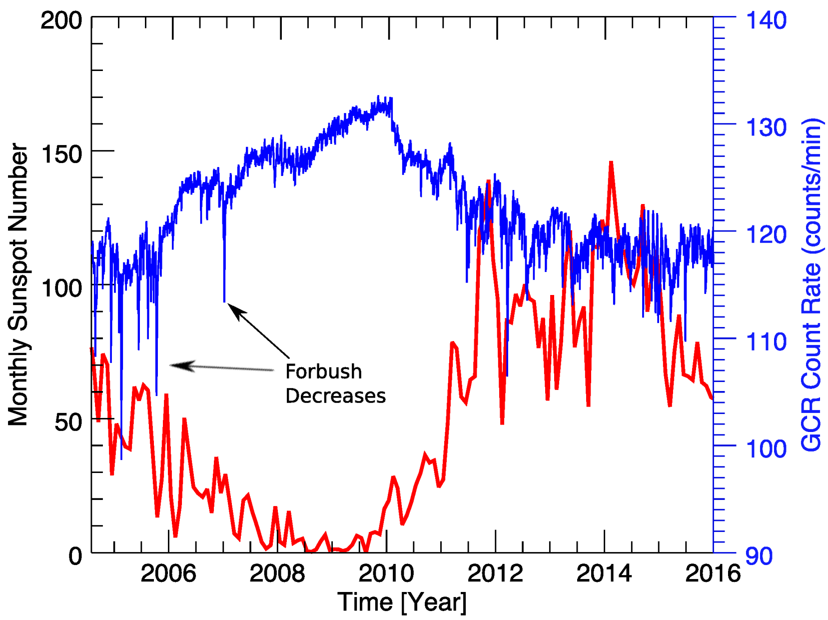

Figure 2: Monthly sunspot number (red) and daily-averaged, neutron monitor count rate (blue), the latter being proportional to the GCR intensity at 1 AU. The data cover the time interval investigated in this study (2004/160 -2016/001). Sunspot numbers are obtained from `http://www.sidc.be/silso/datafiles`, while neutron monitor data are from the Neutron Monitor Database (`http://www.nmdb.eu/nest/`) and the Thulu station at a rigidity of 0.3 GV. The good correspondence of the neutron monitor at Earth readings and GCR measurements at Saturn has been shown in Roussos et al. (2011). The lag between the sunspot minimum and the neutron monitor maximum is indicative of the time required for the solar cycle effects to propagate outward and influence the GCR access throughout the heliosphere.

(Jackman et al., 2008) so the geometry of the west or central meridian observer is probably most relevant. Due to the azimuthal IMF, an east observer at 10 AU is most likely to encounter SEPs in a similar fashion as the west observer at 1 AU. A direct connection of Cassini with a CME in the inner heliosphere is less likely to persist, because of the merging processes and the long IMF line distance involved. As a reference, for solar wind velocities between 500-1000 km/s this distance is in the range of 25-50 AU. SEP travel times from the Sun (t_{SEP}) are between 1.5 and 3 days (5 MeV protons) while shock-travel times (t_S) range between 17 to 35 days. For very fast ICMEs, as the one deriving from a cluster of X-Class flares (the strongest in the classification of solar flares) during January 16-20/2005 (Foullon et al., 2007), t_S of ∼14-18 days were observed (Roussos et al., 2008). On the other hand, the longitudinally broad, merged ICME may allow them to be magnetically connected to the observer for a long duration: the signal of the SEP events described by Roussos et al. (2008) could be resolved up to ∼50 days.

Similarly to (G)MIRs, Corotating Merged Interaction Regions (CMIRs) also form at large heliocentric distances, typically within 15 AU (Burlaga and Ness, 1998). Using Cassini magnetometer observations, Jackman et al. (2008) found that while two magnetic field compressions per solar rotation were typically observed near Saturn, one of the two compression regions was usually much stronger, indicating that the merging of two CIRs into one CMIR per solar rotation has developed significantly by 10 AU. Inverse energy-time dispersion for CIR SEPs may not be relevant at Saturn, since CIR shock strengths are expected to peak within 5 AU (Gosling and Pizzo, 1999).

Statistically, CME and ICME occurrences peak during solar maximum (Webb and Howard, 1994; Wang and N. R. Sheeley, 2015), while CIR frequency is highest during the declining face of the solar cycle, including the solar minimum (Zhang et al., 2008). The Cassini mission spans more than one solar cycle up to 2016 (Figure 2) so that there is no bias in the occurrence of CIR vs ICME driven transients. CIR effects may become more apparent during solar minimum around 2008 and 2009.

3. Instrumentation

3.1. MIMI/LEMMS

The survey for SEP and GCR transients for this study is primarily based on data from Cassini's Low Energy Magnetospheric Measurement System (LEMMS), which is one of the three sensors of the Magnetospheric Imaging Instrument (MIMI) (Krimigis et al., 2004). LEMMS is a charged particle telescope with two units separated by 180° in pointing that are called Low and the High Energy Telescope (LET and HET respectively). Both LET and HET use solid state detectors and coincidence logic to determine the type of particle (electron or ion) and its energy. Furthermore, LET uses magnetic deflection to better separate ions from low energy (<800 keV) electrons.

LEMMS measurements considered here come from several of its "rate" channels. Calibration information is available in Krimigis et al. (2004) and Armstrong et al. (2009). We replicate part of this information in Appendix

C so that the reader can have an immediate access to basic parameters such as channel passbands. The rate channels cover a wide energy range from few tens of keV to tens of MeV. This broad energy response is our primary requirement for detecting and characterizing SEPs.

Protons are measured with A0-A7 and B0-B1 in the LET (28 keV to 1.7 MeV) and P2 - P9 and H5 in the HET (2.42 - 120 MeV). While several of the ion channels capture all Z≥1 ions, we can safely assume that during SEPs their signal is dominated by protons: the ratio of alphas to protons in solar energetic particles rarely exceeds 10% in the energy range of interest (Lario et al., 2003). Ion channels that exclude protons are A8, H1-H4, B2-B3 (Z>1) and Z1-Z3 (Z>8) (Armstrong et al., 2009), measuring heavy ions in the 2.1-193 MeV/nuc energy range. Given the relative abundances of energetic helium, oxygen, carbon and nitrogen in the solar wind (Desai et al., 2006) it is safe to assume that the former group of channels responds to helium and the latter to oxygen. Information from these non-proton measurements will only be added in our survey results for completeness, as these channels are not optimized for detailed SEP composition analysis.

The electron rate channels that we show here is E6 from the HET (>1.6 MeV). As explained in the follow-up paragraphs, these channels are used as indirect tracers of Galactic Cosmic Rays (GCRs) rather than of electrons associated with SEPs. In one occasion we show measurements from LET channels C0-C3 (18-100 keV) in order to identify an interplanetary shock.

LEMMS channels have several sources of background or noise, such as gamma rays from the Radioisotope Thermal Generators (RTGs) of Cassini, sunlight and penetrating energetic particles. For the channels listed above, RTG noise is insignificant. Light contamination affects the LET channels. Instrument penetrating energetic particles are present primarily in the radiation belts of Saturn and during very strong SEP events. Away from the belts the source of penetrating particles are GCRs (Roussos et al., 2011). These define the background count-rate for most of the channels measuring electrons or ions above about 100 keV. When we use the aforementioned background count rate as a GCR proxy, we do not subtract it from the LEMMS measurements. This proxy is important for the characterization of SEP associated disturbances in the solar wind (Section 4) through the detection of FDs.

3.2. Additional datasets

3.2.1. MIMI/CHEMS

CHEMS stands for CHarge and Energy Mass Spectrometer. It is also part of MIMI and can measure the energy, mass and charge state of energetic ions between 3 and 220 keV/e. CHEMS has three wide field-of-view telescopes that in this study we combine in order to improve counting statistics. We use triple coincidence, Pulsed Height Analysed (PHA) event data from CHEMS to distinguish doubly-charged helium (He^{++}) and water group ions (W^{+}) as the former is found in the solar wind while the source of the latter is magnetospheric. Enhanced fluxes or abundance ratios of He^{++} were used in few occasions to characterize the magnetospheric region of Cassini, indicate an active solar wind or validate our LEMMS-based selection of SEP events. We also use CHEMS in a different context within Saturn's radiation belts for one of our example applications (Section 6).

3.2.2. MAG

We will use measurements of the Cassini fluxgate magnetometer (MAG) (Dougherty et al., 2004) in order to identify the magnetospheric region(s) that Cassini crossed during each SEP detection (magnetosphere, magnetosheath, solar wind etc.). We present magnetic field data in the KRTP coordinate system, with R along the line from the center of Saturn to Cassini and positive away from the planet, Phi (ϕ) the azimuthal component parallel to the Kronographic equator and positive in the direction of the planetary rotation. Theta (θ) is the southward component that completes the right-handed system. The resolution of MAG is 4.9 pT for the range of $\pm$ 40 nT that is relevant for the regions of interest in this study.

3.2.3. CAPS

The Cassini Plasma Spectrometer (CAPS) measures the three-dimensional distribution of charged particles with energies between 0.6 eV and 28 keV (electrons) and 1eV/e to 50 keV/e for ions (Young et al., 2004). Similar to the magnetometer, it is used to support the detection and the characterization of an SEP detected by LEMMS and define the magnetospheric region of Cassini at each instant. CAPS data are available until day 154/2012, after which the instrument was switched off. We use data only from its electron component, CAPS/ELS.

3.2.4. RPWS

The Radio and Plasma Wave Science instrument (RPWS) (Gurnett et al., 2004) is used here to obtain electric field spectrograms from 1 Hz to 16 MHz. Earlier studies indicate that the Saturn Kilometric Radiation may extend to low frequencies when a solar storm takes place (Jackman et al., 2010). While we will not survey the RPWS dataset for Low Frequency Extensions, we will demonstrate one such case in one of the applications of Section 6.

4. Detecting SEP and GCR transients

While the detection of SEP and GCR transients with LEMMS has been discussed in past studies, we add few details here for completeness. We refer the reader to Roussos et al. (2008, 2011, 2014) for additional information and examples.

Lario et al. (2004) were the first to review MIMI/LEMMS data in order to identify SEP events. Their survey covered Cassini's interplanetary cruise and the authors used a combination of the instrument's low and high energy electron channels for this task. Near Saturn's magnetosphere, however, energetic particles, especially at the 10s to 100s of keV range, may originate from Saturn (Kollmann et al., 2011; Carbary et al., 2011; Roussos et al., 2016). It is therefore important to make a careful selection of LEMMS channels, the signal of which can be used to track SEPs and GCRs reliably.

Our selections and relevant justification are described in the following two subsections. Essentially, when we survey LEMMS measurements for SEP events we look for intervals that MeV proton enhancements are directly observed. Coincident FDs offer additional, indirect means to identify and characterize SEP transients. Ambiguous candidates are further analyzed using the full capabilities of LEMMS, CHEMS, CAPS and MAG, before we decide whether to include them in our final SEP list. Intervals of periodic FDs are catalogued in a separate list as these may be indicative of CIRs near Saturn.

4.1. SEP transients

LEMMS observations indicate that the only region where LEMMS proton channels P2-P9 measure permanently foreground is inside Tethys's L-shell at L=4.89. The only process that may populate L>4.89 with protons measured by P2-P9 are the transient radiation belts that arise from the interaction of Saturn's magnetosphere with SEP events (Roussos et al., 2008). The signal from these transient structures has been observed to extend up to about L=12. Beyond that, P2-P8 channel rates are nominally at background and may rise above it only during an SEP. Based on the above, we choose channel P2 for our initial survey for SEP events. P2 (2.28 - 4.492 MeV) is the lowest energy, clean proton channel of the HET. Since P-channels in the HET have comparable geometry factors and SEP energy-flux spectra have an inverse power-law distribution, P2 is the channel where we expect the strongest SEP signal.

In order to detect low intensity SEPs we averaged the P2 measurements in time-bins up to one day. In most cases an averaging between 2-8 hours was sufficient. We surveyed the data only outside L=12 in order to avoid the region where transient proton belts may appear. Since we cannot exclude that a very weak, remnant signal from a transient belt may become apparent even outside L=12 after we apply long time averaging to our data, we also check if the profile of a candidate SEP is asymmetric around periapsis: the opposite would be expected for a trapped, magnetospheric population.We also require that an increase in the P2 count-rate persists at least for 2 days and that the increase is higher than the standard deviation of the time-averaged background.

For ambiguous signatures near the detection limit we perform additional checks before we include them in our event list. For instance, we seek for coincident intensity increases in lower energy channels (A5-A7) where the SEP may be stronger, as well as the He^{++} measurements from CHEMS. If Cassini is in the solar wind we can also look for strong enhancements in keV ions measured by A0-A4, where the signature of an SEP event may be more clear (Lario et al., 2004). Examples are shown in Appendix B.

Weak SEP events that are anisotropic in pitch angle may be missed if LEMMS is not pointing at the correct pitch angle, but that is an unavoidable limitation of our survey given that LEMMS scan platform stopped operating early in the mission (day 32/2005). Since, however, most SEP events last for many days or weeks (Section 5.1) during which many pitch angles are covered due to frequent attitude changes of Cassini, we believe that this limitation had a small impact in our survey results.

4.2. GCR transients and periodicities

Excluding the radiation belts, GCRs variations can be tracked with channels P9, E6, E7, B2, B3, H3-H5, Z1-Z3 that receive negligible foreground even

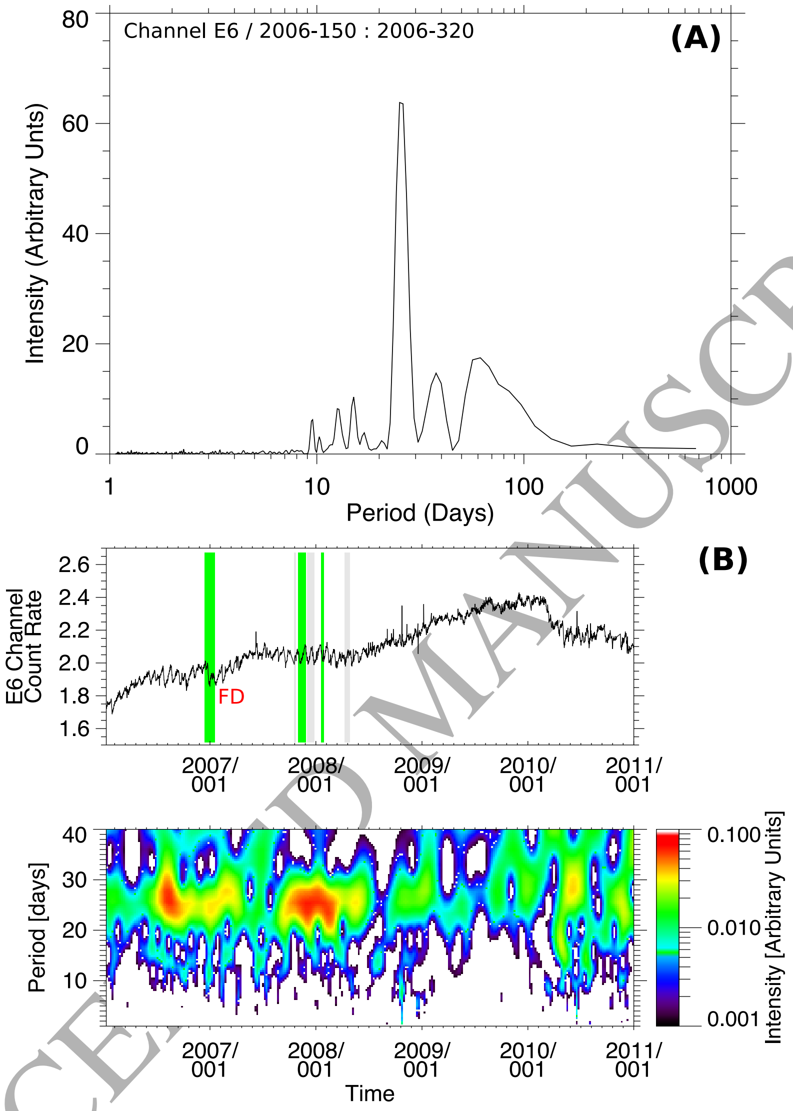

Figure 3: (A) Lomb-Scargle periodogram of LEMMS E6 count-rates obtained between days 150-320 of 2006 (B) The top panel shows time series of LEMMS E6 channel count-rates. Shaded areas mark SEP events where the alternating colors are only used to better distinguish adjacent events. An FD is also identified for one of those events. The bottom panel shows the corresponding wavelet spectrogram, where times of clear solar periodicity can be identified.

during the strongest SEPs. E6 data are shown here, mainly due to the channel's relatively high-sensitivity to GCRs. Averaging background rates for 6-8 hours is usually sufficient to resolve the GCR time-series and the profile of FDs (Roussos et al., 2011). Longer averaging is also possible but that may smear an FDs structure (e.g. stepped decrease) which can be indicative of whether the FD is associated with an interplanetary shock, an ICME or both.

Recurrent FD intervals are first identified manually, after which we apply a Lomb-Scargle analysis to quantify the dominant period and the date range to which periodic behavior is contained. As we are primarily interested in solar periodicities, we mainly seek for peaks in the Lomb-Scargle periodograms at 13 and 26 days. To reduce ambiguity of our selections, we also apply a wavelet transform in the GCR time series. Doing that requires to interpolate the LEMMS measurements to a uniform sampling rate, but that has a negligile effect on the results, as measurements are nearly continuous and data gaps are shorter than one day. Sample results are shown in Figure 3.

The top panel (A) shows the Lomb-Scargle periodogram applied on the E6-channel time series for days 150-320 of 2006. A peak at the solar rotation period of 26 days is clearly visible. The bottom panels (B) show time series of channel E6 for a longer time interval (2006-2011) and the corresponding wavelet spectrogram, showing clear enhancements at the solar rotation period for several extended time intervals between 2006 and 2009. Shaded areas on the E6 time series mark SEP events identified using the principles described in Section 4.1. One of these SEPs is clearly associated with an FD, which is also marked. The wavelet spectrum can be noisy even for intervals that a solar periodicity is clearly visible (e.g. ealry 2006), which justifies the use of two methods in a complementary sense.

5. Event lists

Our survey covers the time period between day 160/2004 and the end of 2015. We provide two event lists: one for SEP events and one for intervals were solar periodicities are identified in GCRs.

5.1. SEP and GCR transients

Tables 1-3 list all the SEP events identified based on the principles described and demonstrated in Section 4. Plots with LEMMS data from channels P2, P3 and E6 for the corresponding intervals are shown in Appendix B. Several details regarding the information in Tables 1-3 are given below:

Event numbering: We assign a unique number to each SEP event. There are several cases with adjacent SEP that could also be considered as a single entity (e.g. events 8-9, 20-21, 34-35). We catalogue adjacent events as separate if we can distinguish two peaks in the SEP's ion count-rate profile or more than one FDs within this extended time interval. Each interval is color coded with red, green, blue or grey, according to the signal to noise ratio (SNR) of each event in channel P2 at the time of the SEP's peak. The noise here is defined as the GCR background noise of P2. Red corresponds to SNR>10, green to 2.5<SNR<10, and blue to SNR<2.5. Grey color is used for ambiguous detections. During the time of event 14, for instance, a subtle increase is visible in the count-rate of P2, following, however, an extended LEMMS data gap that precludes an SEP identification with certainty.

Start/Stop dates: The two entries indicate the start and stop date of each event. The accuracy that we can detect the two dates depend on how data are averaged, which channels are used for identification and what count-rate threshold is chosen for defining the onset/end of an SEP. For that reason, start and stop dates for most SEPs can be uncertain by 1-3 days, excluding SEPs that peak impulsively (Figure 1) the onset of which may be defined with an accuracy of less than a day (e.g. SEP event 31).

Peak time: The peak time is defined as time that LEMMS channel P2 measures the highest count rate of an SEP. The time is automatically retrieved and rounded up to the closest hour of day. If the SEP is not resolved in channel P2, we use channels A7 or A6. For this reason we refer the reader to the plots of Appendix B for additional clarification on what the peak time actually represents.

Forbush Decrease: In this column we define whether we identify an FD that can be associated with a given SEP. Identification of an FD is sometimes unclear due to the solar periodicity in the GCR-induced LEMMS background, in which case we the column entry is *"Maybe"*.

LEMMS ion channels: After an SEP is identified with channel P2 or other indirect methods (Section 4), we review all LEMMS ion channels and list which of those may be showing an SEP contribution. We distinguish the LEMMS channels according to the ion species they may respond to based on the arguments described in Section 3. Only few of the strongest ("red") SEPs have a signal in the non-proton channels. The lack of a signal in the non-proton MeV channels in many events is likely due to their low sensitivity, as their geometry factor is more suitable for measurements in the radiation belts. When an SEP is visible in channels A0-A7, the measured signal may be a mix of magnetospheric and solar wind ions, especially in A0-A4.

Region: Here we identify the magnetospheric interaction regions crossed by Cassini between the start and stop dates of an SEP. "SW" stands for "Solar Wind", "MSH" for "Magnetosheath" and "MSP" for "Magnetosphere". Each of the regions noted may have been crossed multiple times for a given SEP event, as several SEPs last over two or three Cassini periapses (e.g. events 9, 10) or because of magnetopause/bow-shock oscillations. For the identification of the different regions we rely on the magnetopause crossings list by Pilkington et al. (2015) and our survey of MAG and CAPS data.

Notes: Here we add several short notes that could be of importance for an SEP but do not fit in any of the other columns. The list of notes is not exhaustive about the features of an SEP and the corresponding magnetospheric interaction signatures, but may serve as starting points or guidelines for case studies of individual events. Complementary information is also provided in Table 5 of Section 7.

Using the information in Tables 1-3 (and the corresponding plots in Appendix B), we can add several important points:

1. No SEPs have been identified in 2009 and 2010 while the SEPs of 2008 are very weak in intensity, which may correspond to strong CIRs observed at 1 AU (Bučík et al., 2011). The result is consistent with the expectations for an extended solar minimum between 2008 and 2010, assuming that most of the observed SEP events in our survey period are associated to ICMEs and their shocks rather than CIRs. Our findings have a good correspondence to a similar SEP occurrence minimum observed at 1 AU (`https://umbra.nascom.nasa.gov/SEP/`). This observation serves as a minimal validation of our survey results.
2. About 94% of SEP events last at least one week, while 74% have a duration exceeding two weeks. That is additional evidence that most

	SEP Dates (Year-DOY)			Forbush	LEMMS Ion Channels			Region	Notes
	Start	Peak Time	Stop	Decrease	H^+	He^{n+}	O^{n+}		
1	2004-210	2004-239T01:00	2004-252	Yes	A1-A7 P2-P3	--	--	SW	1) Jackman et al. (2005) 2) Shocks: end of day 207, day 232, day 247 3) Multiple HCS crossings
2	2004-260	2004-271T01:00	2004-288	No	A1-A7 P2-P4	--	--	SW	1) Extended compression during days 260-270
3	2004-322	2004-338T13:00	2004-350	Yes	A1-A7 P2-P6	A8 H1	--	SW, MSH, MSP	1) CIR compression day 322 2) CIR compression coincident with SEP peak 3) HCS crossing, day 338
4	2005-021	2005-034T11:00	2005-046	Yes	A2-A7 P2-P8	A8 H1-H3 B2-B3	Z1	SW, MSH	1) Roussos et al. (2008) 2) X7.1 flare (Foullon et al., 2007)
5	2005-055	2005-060T18:00	2005-067	No	A2-A7 P2-P3		--	SW, MSH	1) Roussos et al. (2008)
6	2005-083	2005-085T01:00	2005-087	Yes	A4-A7 P2-P3	--	--	SW, MSH	1) Roussos et al. (2008) 2) Rarefied SW (days 80-84) 3) Compressed SW days 84-86
7	2005-142	2005-151T13:00	2005-159	Yes	A4-A7 P2-P3	--	--	SW, MSH, MSP	1) Roussos et al. (2008) 2) No CAPS after day 145
8	2005-203	2005-208T06:00	2005-212	No	A4-A7 P2-P6	--	--	SW, MSH, MSP	1) Roussos et al. (2008) 2) Rarefied SW (days 206-209)
9	2005-213	2005-224T16:00	2005-240	Yes	A3-A7 P2-P8	A8 H1-H2 B2-B3	--	SW, MSH, MSP	1) Roussos et al. (2008) 2) 2 periapses
10	2005-243	2005-258T23:00	2005-292	Yes	A0-A7 P2-P9	A8 H1-H4 B2-B3	Z1-Z2	SW, MSH, MSP	1) Roussos et al. (2008) 2) 3 periapses
11	2005-310	2005-313T13:00	2005-317	No	A3-A7 P2	--	--	MSH, SW	1) Short solar wind excursions
12	2006-001	2006-002T00:00	2006-003	Maybe	A3-A6	--	--	MSH, SW	1) CHEMS based 2) detection
13	2006-346	2006-355T08:00	2007-017	Yes	A4-A7 P2-P6	H1-H2	--	SW, MSH, MSP	1) 3 periapses 2) Elevated lobe field (e.g. days 7-11)
14	2007-292	2007-297T23:00	2007-298	No	P2	--	--	MSH, MSP	1) Noisy magnetic field in and out of the MSP
15	2007-306	2007-316T04:00	2007-332	Maybe	A0-A7 P2	--	--	SW, MSH, MSP	1) HCS crossing (days 307-310)
16	2007-335	2007-353T18:00	2007-360	No	P2-P3	--	--	SW, MSH, MSP	1) 2 periapses 2) Data gaps (day 346-348, 355-358)
17	2008-018	2008-027T04:00	2008-028	Maybe	A4-A7 P2	--	--	SW, MSH, MSP	1) MAG data gap up to day 24

Table 1: List of SEP events and some of their basic characteristics (see Section 5 for explanation). Color-coding of event numbers refers to their intensity: red for SNR>10, green for 2.5<SNR<10, and blue for SNR<2.5. Grey color is used for ambiguous detections. More events are listed in Tables 2 and 3.

	SEP Dates (Year-DOY)			Forbush	LEMMS Ion Channels			Region	Notes
	Start	Peak Time	Stop	Decrease	H^+	He^{n+}	O^{n+}		
18	2008-099	2008-102T04:00	2008-117	Maybe	A7 P2-P3	--	--	SW, MSH, MSP	1) 2 periapses 2) Strong | B | compression before SEP (day 97)
19	2011-081	2011-094T04:00	2011-106	Yes	A4-A7 P2-P4	--	--	SW, MSH, MSP	1) Compressed SW around SEP peak (days 93-97) Solar-wind driven auroral storm (Meredith et al., 2014)
20	2011-159	2011-172T08:00	2011-187	Yes	A3-A7 P2-P6	--	--	SW, MSH, MSP	1) SEP peak around periapsis
21	2011-189	2011-190T18:00	2011-197	Maybe	P2-P3	--	--	SW, MSH, MSP	1) Rarefied SW (all times after day 194)
22	2011-279	2011-286T11:00	2011-307	Yes	A4-A7 P2-P4	--	--	SW, MSH, MSP	1) Rarefied SW (days 278, 282-284)
23	2012-031	2012-053T23:00	2012-069	Yes	A4-A7 P2-P4	--	--	SW, MSH, MSP	1) SEP peak around periapsis 2) Sharp entry into SW ~1 day after SEP peak
24	2012-070	2012-097T13:00	2012-106	Yes	A0-A7 P2-P6	A8 H1	--	SW, MSH, MSP	1) 3 periapses 2) Possible IP shock (day 73)
25	2012-162	2012-163T08:00	2012-170	Yes	A4-A7	--	--	SW, MSH	1) Rarefied SW
26	2012-205	2012-206T18:00	2012-209	Maybe	P2-P3	--	--	SW, MSH, MSP	1) SEP peak around periapsis and MP crossing 2) Steady field inbound, fluctuating outbound after SEP arrival
27	2012-212	2012-228T16:00	2012-246	Yes	A4-A7 P2-P6	--	--	SW, MSH, MSP	1) 2 periapses 2) SEP peak around periapsis
28	2012-271	2012-281T16:00	2012-287	Maybe	A4-A7 P2	--	--	SW, MSH, MSP	1) Short SW and MSH encounters
29	2013-151	2013-160T04:00	2013-177	Yes	A3-A7 P2-P4	--	--	MSH, MSP	1) 3 periapses
30	2013-248	2013-258T06:00	2013-267	Yes	A5-A7 P2-P3	--	--	MSH, MSP	1) Enhanced | B | in lobe (days 248-253) 2) Enhanced | B | in magnetotail (after day 259)
31	2013-330	2013-332T23:00	2013-345	Yes	A0-A7 P2-P5	A8 H1	--	MSH, MSP	1) Sudden dropouts in | B | (days 330-332) 2) Strong | B | enhancement and rotation at SEP peak 3) Enhancd | B | in lobe (days 337-342) 4) T96 flyby in the SW (Bertucci et al. 2015)

Table 2: Same as Table 1 for events 18-31

	SEP Dates (Year-DOY)			Forbush	LEMMS Ion Channels			Region	Notes
	Start	Peak Time	Stop	Decrease	H^+	He^{n+}	O^{n+}		
32	2014-015	2014-025T01:00	2014-038	Yes	A6-A7 P2-P4	--	--	MSH, MSP	1) Enhanced | B | after SEP arrival (days 17-18)
33	2014-073	2014-077T18:00	2014-090	Maybe	A5-A7 P2-P4	--	--	SW, MSH, MSP	1) Enhanced | B | in lobe (days 72-77)
34	2014-238	2014-260T11:00	2014-269	Maybe	A5-A7 P2-P9	--	--	SW, MSH, MSP	1) SEP peak around periapsis 2) Enhanced | B | in lobe (days 266-270)
35	2014-270	2014-272T23:00	2014-285	Maybe	A3-A7 P2-P4	--	--	SW, MSH, MSP	1) Short SW and MSH encounters
36	2014-318	2014-319T23:00	2014-324	Yes	A4-A7 P2-P3	--	--	SW, MSH	1) Signature of strong shock (day 322) 2) HCS crossing (days 321-322) 3) Witasse et al. (2017)
37	2014-346	2014-358T08:00	2015-001	Yes	A0-A7 P2-P7	--	--	SW, MSH, MSP	1) Enhanced | B | in lobe (days 346-355)
38	2015-001	2015-007T18:00	2015-025	Yes	A4-A7 P2-P4	--	--	MSH, MSP	1) SEP peak around periapsis 2) Enhanced | B | in lobe (days 13-23)
39	2015-026	2015-034T08:00	2015-040	Maybe	A4-A7 P2-P3	--	--	MSH, MSP	1) Lack of enhancement in | B | of lobe
40	2015-041	2015-044T23:00	2015-057	No	A4-A7 P2-P3	--	--	MSP	1) Enhanced | B | in lobe (days 45-60)
41	2015-058	2015-066T18:00	2015-072	No	A4-A7 P2-P4	--	--	MSH, MSP	1) Sheath encounters frequent around SEP peak (days 65, 67-70)
42	2015-073	2015-086T18:00	2015-097	Yes	A4-A7 P2-P3	--	--	MSP	1) Enhanced | B | in lobe (days 78-86)
43	2015-101	2015-113T23:00	2015-117	Yes	A0-A7 P2-P3	--	--	MSP	1) Enhanced | B | in lobe (days 201-205) 2) Noisy magnetic field after SEP peak
44	2015-131	2015-138T11:00	2015-145	Maybe	A4-A7 P2	--	--	MSH, MSP	1) Enhanced | B | in lobe (days 132-141) 2) Possible sheath excursions at 40 Rs (days 141-143) although Cassini at ∼04:00LT
45	2015-186	2015-197T11:00	2015-208	Yes	A0-A7 P2-P4	A8 H1	--	MSH, MSP	1) Noisier field compared to similar orbits 2) Enhanced | B | in lobe (days 191-195)
46	2015-358	2015-361T18:00	2016-001	No	A4-A7 P2-P3	--	--	MSH, MSP	1) Moderately enhanced tail field

Table 3: Same as Table 1 for events 32-46

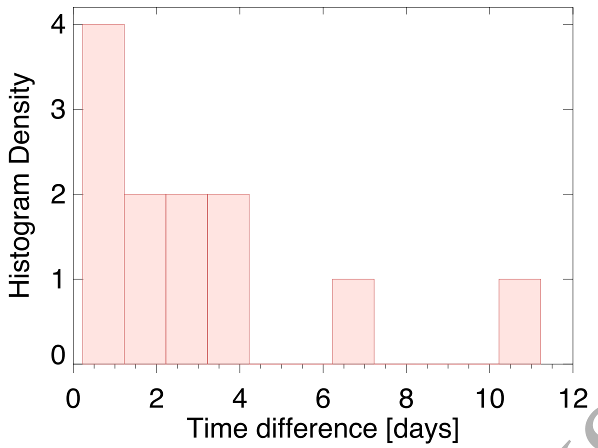

Figure 4: Histogram of time differences ($\Delta\, t$) between the onset of two-step FDs and the peak count-rate of the corresponding SEP event. The size of the bins is one day.

of the events catalogued are associated to ICMEs rather than CIRs, since the time-scale of CIR magnetic field compressions at 9-10 AU is about a week (Jackman et al., 2004, 2008), while CIR energetic particles are seen typically 2-3 days outside of a CIR compression region (Bučík et al., 2009).

3. 54% of SEPs are associated with strong FDs, indicating the crossing of an interplanetary shock, the ICME or both. The percentage may be higher because identification of FDs is ambiguous in 11 more events (24%).
4. 12 out of the 23 SEP events with strong FDs show evidence for two step decrease (3, 4, 9, 13, 20, 24, 26, 29, 31, 32, 36, 43), where a first dropout driven by an interplanetary shock is enhanced by a second decrease due to the passage of the ICME (see also example plots in Appendix D). As the first step provides the approximate shock crossing time, we can estimate its time separation from the SEP peak ($\Delta\, t$). Figure 4 shows the distribution of $\Delta\, t$. Most values are within 1 day, and 83% of the cases has a $\Delta\, t < 4.1$ days. The two extremes are for events 4 and 32 that the SEPs have complex structures (e.g. multiple peaks) and the corresponding FDs more than two steps. We still observe that one of the FD steps occurs within a day from those SEP peaks.
5. In several of the events showing a two-step FD we can directly observe

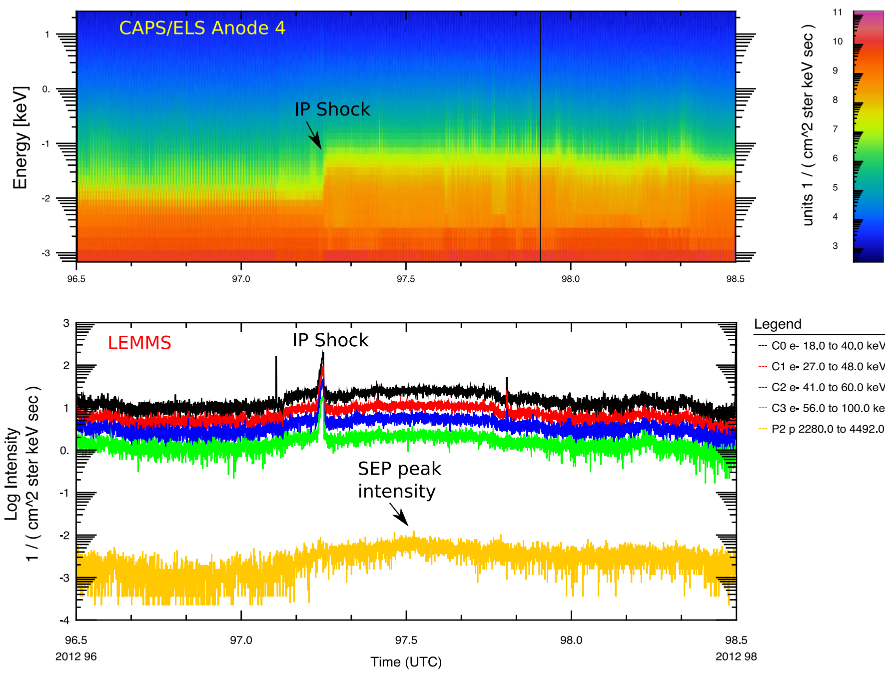

Figure 5: CAPS/ELS spectrogram (top) and LEMMS keV electron and MeV proton intensities shown an interplanetary (IP) shock associated with SEP 24. The timing of the peak intensity of LEMMS P2 channel ions is observed several hours after the shock crossing. A weaker peak is visible in P2 channel at the time of the shock, that is stronger in lower energy LEMMS and CHEMS ion channels (not shown).

the interplanetary shock with CAPS, MAG, LEMMS or CHEMS and compare with the inferred value based on the FD onset. For event 24 (Figure 5), the shock is seen around 06:00 on day 97/2012 while the time inferred based on the FD was between 08:00 and 11:00 of the same day. For event 31 (Section 6.2) the shock is seen with MAG on day 332/2013 at 21:00. The FD-based time is between 00:00-04:00 on day 333/2013. Finally, the shock for event 36, MAG data indicate a shock crossing at 18:55 on day 336/2014, while the FD onset is between 00:00-06:00 on day 337/2014. These time differences are comparable to the averaging time we apply to the LEMMS data in order to resolve the GCR time series with a good signal over noise.

6. The intensity of four SEP events (10, 37, 38, 45) with a single-step FD peaks within 5 days from the FD onset. Furthermore, in none of the events could we observe a strong energy-time dispersion in the SEP peak.
7. Based on points 4-6, we conclude that the peak intensities of the strongest SEPs observed with LEMMS occur within ∼4 days of the crossing time of an interplanetary shock, the enhanced IMF within the ICME or both. That is consistent with a crossing geometry similar to that of a central meridian or west observer, as described in Section 2. The crossing time of the shock or the compressed IMF can be refined to less than half a day through the FD onset. This provides a good starting point for pinpointing the timing of solar wind disturbances through a dedicated analysis of each event individually, a task that is beyond the scope of the current study.
8. Weak intensity SEP events which are not accompanied by strong FDs (e.g. 1, 6, 7, 12, 14, 15, 17, 18, 44) may be observed due to a distant magnetic connection with a shock/ICME or originate at CIRs, as we discuss in Section 5.2.

5.2. Intervals of periodic GCR variations

Table 4 lists intervals that a solar periodicity in GCRs was identified based on the analysis method described in Section 4. Plots where periodic variations of GCRs can be visualized are shown in Figure 3 and the bottom panels of the plots in Appendix B. Similar to Section 5.1, we provide a description of the different columns of Table 4 below:

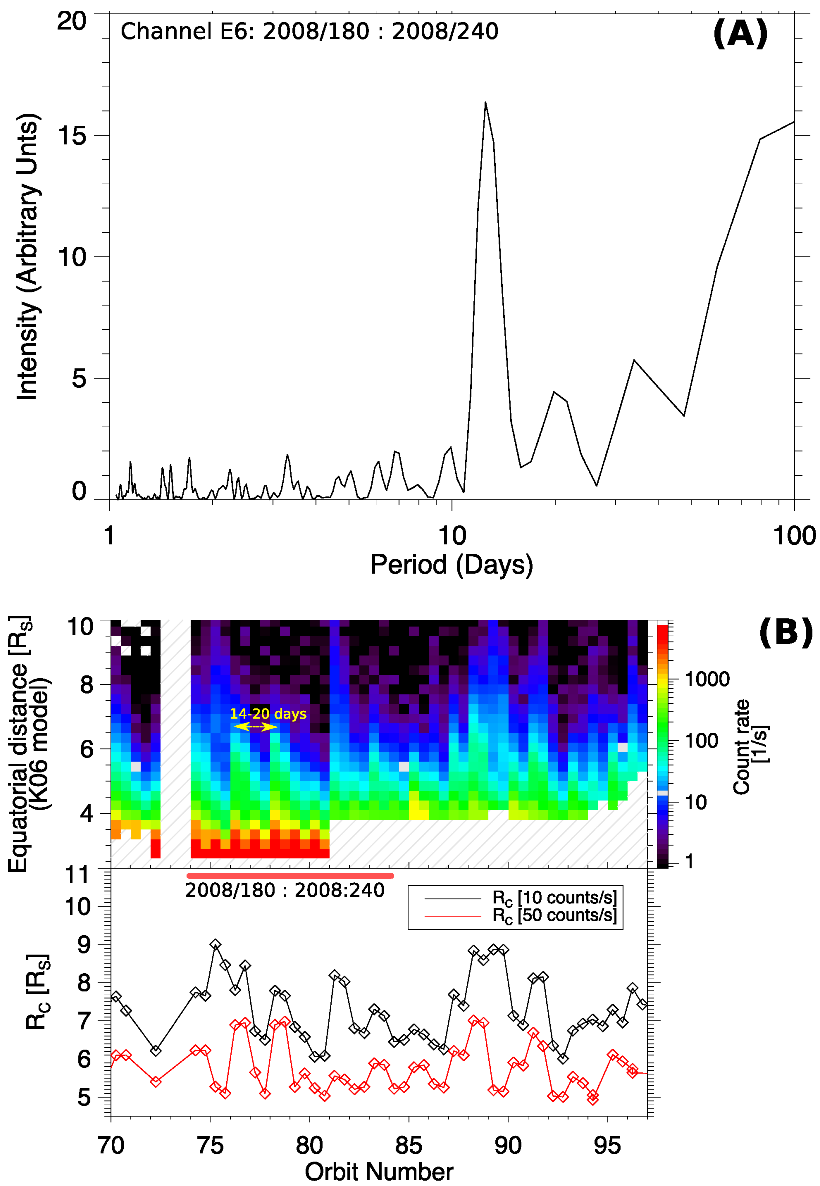

Figure 6: (A) Lomb-Scargle periodogram of LEMMS E6 count-rates obtained between days 180-240 of 2008 (B) Orbit-distance spectrogram of >1 MeV electron count-rates in Saturn's radiation belts (top) and the electron belt extension, R_C (bottom), given as a distance that a selected count-rate levels are measured. The plot is adopted from Roussos et al. (2014), with a red bar added to mark the interval of the 13-day periodicity in GCRs.

Event numbering: This is a unique number assigned to each periodic GCR interval. Some events may be considered as continuous but we separate them when continuity appears to be disrupted by an SEP (e.g. events 4, 5) or when extended data gaps are present (e.g. events 6, 7).

Start-stop days: The beginning and end date of each periodic GCR interval. These can be uncertain by 10-15 days, which is why the list includes intervals >50 days.

Period: The dominant time period resulting from a Lomb-Scargle analysis. The uncertainty is about 1 day for the strongest events and about 4 days for ambiguous events. Some cases may show double peaks near 13 and 26 days (e.g. interval 11 - see also Figure 3) but due to ambiguity we only refer to the strongest peak here.

Notes: Here we add any additional information not belonging to the other columns, such as SEP events from 1-3 that fall within a given interval or relevant references.

Based on Table 4 we add the following points:

1. Out of the 18 SEP events that occur within the Table 4 intervals, 15 are of low intensity and five have a duration up to 10 days, which can be comparable to the time-scales of CIR compressions (Jackman et al., 2004, 2008). No energy-time dispersion is observed for any of the 15 events. Based on the above, a considerable fraction of these SEP events may result from particle acceleration at CIR shocks, but whether this is the case requires a separate analysis for each event, a task beyond the scope of this study.
2. Most periodic intervals occur before 2010, with the strongest ones during the declining phase of the solar cycle, as expected for CIRs (Webb and Howard, 1994). It is, however, possible that the source of solar periodicity in GCRs is not local, but distant and is observed due to energetic particle transport processes in the heliosphere. For instance, studies based on Ulysses measurements indicated that the same 26-day periodicity exists at high heliospheric latitudes, although longer periods were expected due to the differential solar rotation Simpson (1998).
3. Interval 7 is the only case found that we could resolve dominant periodic GCR variations at half the solar rotation period, which is typical for two

	Start time	Stop Time	Period (days)	Notes
1	2004-200	2004-250	29	(Jackman et al., 2004, 2008) SEP: 1
2	2005-040	2005-140	24	(Jackman et al., 2008; Roussos et al., 2011) SEPs: 5-6
3	2005-350	2006-050	24	SEP: 12
4	2006-150	2006-320	26	—
5	2007-040	2007-100	26	—
6	2007-210	2007-280	25	—
7	2007-290	2008-150	25	SEPs: 14-18
8	2008-180	2008-240	13	(Roussos et al., 2014)
9	2008-240	2008-350	26	—
10	2009-240	2009-320	26	—
11	2010-090	2010-220	28	—
12	2011-130	2011-240	25	SEPs: 20-21
13	2013-060	2013-150	24	—
14	2013-170	2013-290	29	SEP: 29
15	2014-200	2014-320	23	SEPs: 34-36
16	2015-090	2015-140	28	SEP: 42-44
17	2015-280	2015-330	28	—

Table 4: List of intervals with solar periodicity ($sim13$ or 26 days) in LEMMS measurements of GCRs. Events color-coded with red have the strongest peak in Lomb-Scargle periodograms, while the ones with grey are ambiguous. SEP events that fall within a given interval are listed in the last column, together with some relevant references.

CIRs per solar rotation (Jackman et al., 2004). Interestingly, Roussos et al. (2014) reported a similar periodicity in the expansion of Saturn's electron radiation belts for the same time period. We reproduce this result in Figure 6, where panel (A) shows the clear, ∼13-day peak in periodogram of GCRs, while in panels (B) we show the Orbit-distance spectrogram of >1 MeV electron count-rates in Saturn's radiation belts (top) and the electron belt extension (bottom). The belt extension is defined as the distance that a selected count-rate level is measured and here we show two such levels. A red bar marks the interval that the 13-day period is seen in GCRs. A Lomb-Scargle analysis indicated a radiation belt boundary variation at a period of 14-20 days. As it is natural to have a delay between a solar wind induced disturbance and a response of the radiation belts (Miyoshi and Kataoka, 2008), we suggest that CIRs recurring every ∼13 days are the driver of the electron belt modulation. Furthermore, this correlation can only exist if the source of the GCR periodicity is from distant but from local CIRs.

4. Two IMF compressions identified in 2004 (Jackman et al., 2004, 2008) are contained within GCR minima around days 214 and 236 of the same year, also indicating that the solar modulation of GCRs is driven by local CIRs. If that is the case, GCRs measured with LEMMS could provide a continuous monitoring of the phase of SW compressions and rarefactions during any of the Table 4 intervals.

6. Applications

In this Section we demonstrate the utility of the event lists for providing context to Cassini observations. Two applications are presented: (a) the detection and formation of transient radiation belts and (b) compressions of the magnetospheric lobe fields.

6.1. Transient radiation belts

The case for transient ion radiation belts was initially discussed in Roussos et al. (2008): following the strong SEP events of 2005 (events 4, 9, 10) a new component of Saturn's proton radiation belts was observed between the L-shell of Tethys (L=4.89) and L∼10. The belts' intensity decayed to background levels within several months as inwardly diffusing protons crossing the L-shell of Tethys where getting absorbed by that moon. No enhancement has been observed in the proton belts inward of Tethys (at least above

2.28 MeV), indicating that the inner MeV proton belts are supplied through secondary particles of GCR impacts with the rings and atmosphere and are isolated from the rest of the magnetosphere (Kollmann et al., 2013). Contrary to that, the electron belts show significant variability. A first survey by Roussos et al. (2014) indicated that the correspondence between several strong SEP events identified at that time and the intensifications of the electron radiation belts was not unique. With the event list of Tables 1-3 in mind, we revisit some of these findings in an attempt to understand the conditions and the process under which transient ion and electron radiation belts form.

Figure 7 shows color-coded intensities of 2.28-4.92 MeV protons (top) and 1.6-21.0 MeV electrons (bottom) for Cassini orbits 115-170 (2009/168 - 2012/192) and as a function of the dipole L-shell. Proton belts inside L=4.89 remain stable for the almost all the plotted interval. No obvious response is seen in the belts following events 20-23. The SEPs fill the magnetosphere with MeV ions down to L$\sim$8. Penetration to lower L-shells has been slowed by Saturn's magnetic field and no transient radiation belt is visible. Electron belts are more variable but no obvious link to SEP events 20-23 is seen.

On the other hand, a transient radiation belt in both MeV electrons and protons appears as a response to SEP event 24. The transient belt was observed during the periapsis of day 105/2012. What is even more significant is that for the first time we can detect that such a belt has a small but detectable effect on the outer edge of the MeV proton radiation belts, inside L=4.89. This rare event is an indication that fast radial transport occurred in association to SEP 24 and the formation of the transient radiation belt. Below we review LEMMS observations against our SEP event list in order to answer why this was not the case for events 20-23.

Transient radiation belts have been observed in association with events 4, 9, 10 and 24. These, together with events 20 and 31 are the strongest SEPs we have identified. At the time of event 31, Cassini's periapsis was far from the inner magnetosphere and we cannot assess if a transient radiation belt appeared or not. For event 20 the periapsis was at L=5.8.

What we realize is that for events 4, 9, 10 and 24, the SEP peaks *preceded* the transient radiation belts' observation by $\sim$8-12 days. Most notably, while events 10 and 24 span three periapsis crossings in duration, the transient belts appeared only in the orbits following each SEPs peak. Clearly, the SEP peak marks an important time period associated with the dynamical processes forming the transient radiation belts.

Since our analysis indicates that the peak intensity of strongest SEPs is

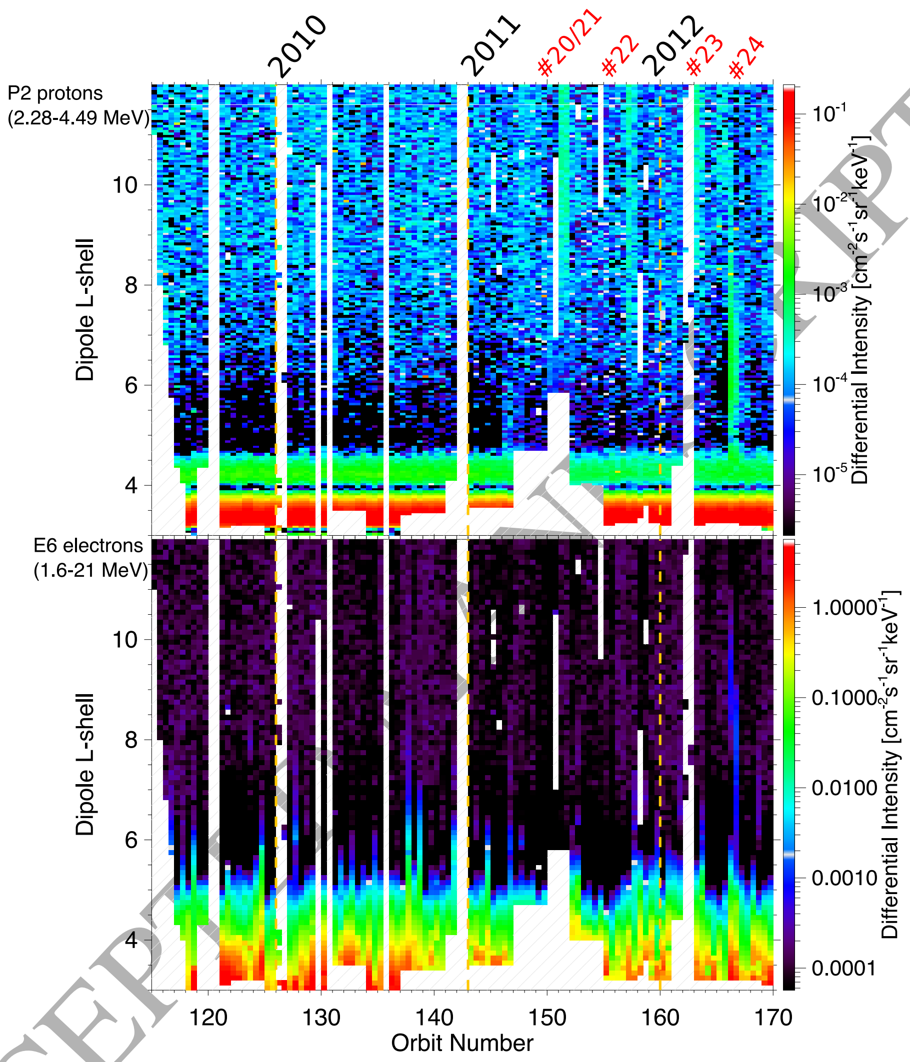

Figure 7: Color-coded fluxes of ion channel P2 (top) and E6 (bottom) as a function of orbit number and dipole L-shell. We define the orbit number starting with 1.0 the day before SOI and increasing by 0.5 every periapsis and apoapsis (i.e orbit 1.5 is the outbound SOI orbit post-periapsis), as used in Roussos et al. (2014). Note that this is not the official designation used for orbit numbering from the Cassini project. Changes of the years are indicated (dashed orange lines), and SEP event numbers are marked in red. Abrupt changes in the electron count-rates is partly due to Cassini rotations and the much stronger pitch angle dependence of E6-channel electrons compared to P2-channel protons.

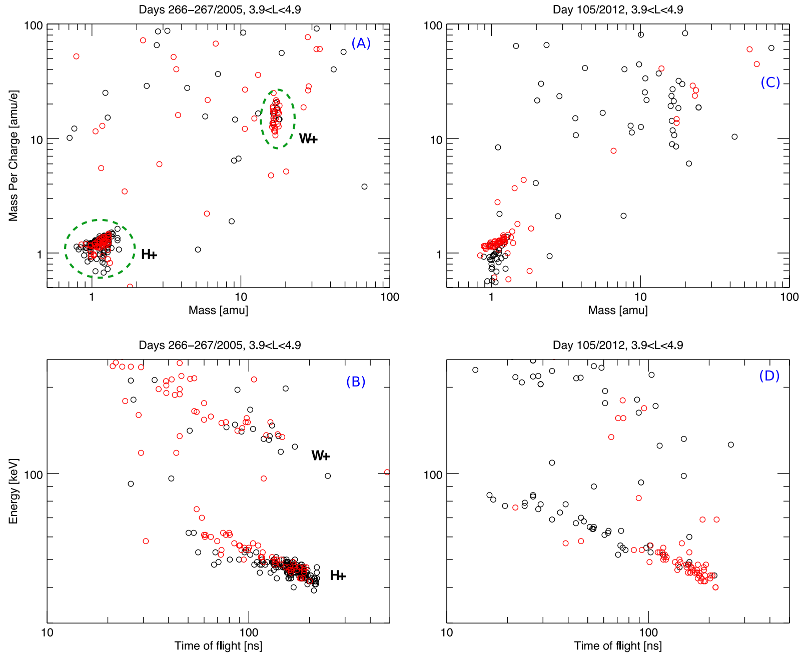

Figure 8: Mass per charge-Mass and Energy-Time of Flight event matrices for 30-220 keV/e protons and 60-220 keV/e for water group ions and for the L-shell range between Enceladus and Tethys where CHEMS is usually at background (Paranicas et al., 2008). (A) and (B) are for the periapsis following the peak of event 10, (C) and (D) for the orbit following the peak of event 24. The signature of protons is clear in both cases, as they form clear groups of data points or tracks, traces of water group ions are also visible (better on the left panels). Scattered points are from accidental coincidences (instrument penetrating particles). Black points are for the inbound portion of the orbit, red for the outbound.

within few days of the associated interplanetary shock (Figure 4) and the shock has been directly observed in one of these cases (Figure 5), we believe that the absence of a transient radiation belt appearance following event 20 is because its peak of that event (and likely the shock) occurred three days *after* the periapsis of day 169/2011. In addition, the next periapsis was $\sim$20 days later (day 192/2011). While a transient belt that could have formed shortly after the shock, there was enough time for it to be absorbed at Tethys before Cassini's next periapsis.

Based on that, we suggest that shock-induced magnetospheric interaction enhances radial plasma transport on global scales that enables the rapid transfer and adiabatic heating of SEPs from L$\sim$8 (where they can directly penetrate, as we can see for events 20-23), to the inner magnetosphere. Similar processes have been observed and modeled for the Earth's magnetosphere (Hudson et al., 1995, 1997; Sarris et al., 2002). The concept of enhanced radial transport is consistent with the rare observation of MeV ions crossing Tethys's L-shell that we identified earlier.

What further supports our inference that shock-induced transport is part of the mechanism forming transient radiation belts is that CHEMS data inside Tethys's L-shell (3.9<L<4.89) for days 266/2005 (after event 10) and 105/2015 (after event 24) reveal that energetic ions have penetrated into a region where ion fluxes are commonly below the detection limit (Figure 8). These measurements show also traces of water group species, the origin of which is magnetospheric and not from SEPs. Dialynas et al. (2009) estimate that lifetimes of $\sim$100 keV oxygen and protons against charge-exchange in the neutral torus range between few hours and few days, respectively. In that sense, the rapid energetic particle transport at Saturn is required in order to minimize the particle losses as particles convect inwards and get energized, forming the transient radiation belts.

6.2. Magnetospheric field compressions

Jackman and Arridge (2011) established a baseline radial profile for the average magnetic field strength of Saturn's magnetospheric lobes. Deviations from this baseline may be used to identify time periods that the magnetosphere is compressed or inflated, but cannot reveal the driver behind such deviations. Here we present a case where we can link a lobe field compression to solar wind processes associated to SEP event 31, shown in Figure 9.

SEP event 31 is among the strongest in our list with a well-defined peak which occurred between 19:00 and 21:00 on day 332/2013. Precursor SEP

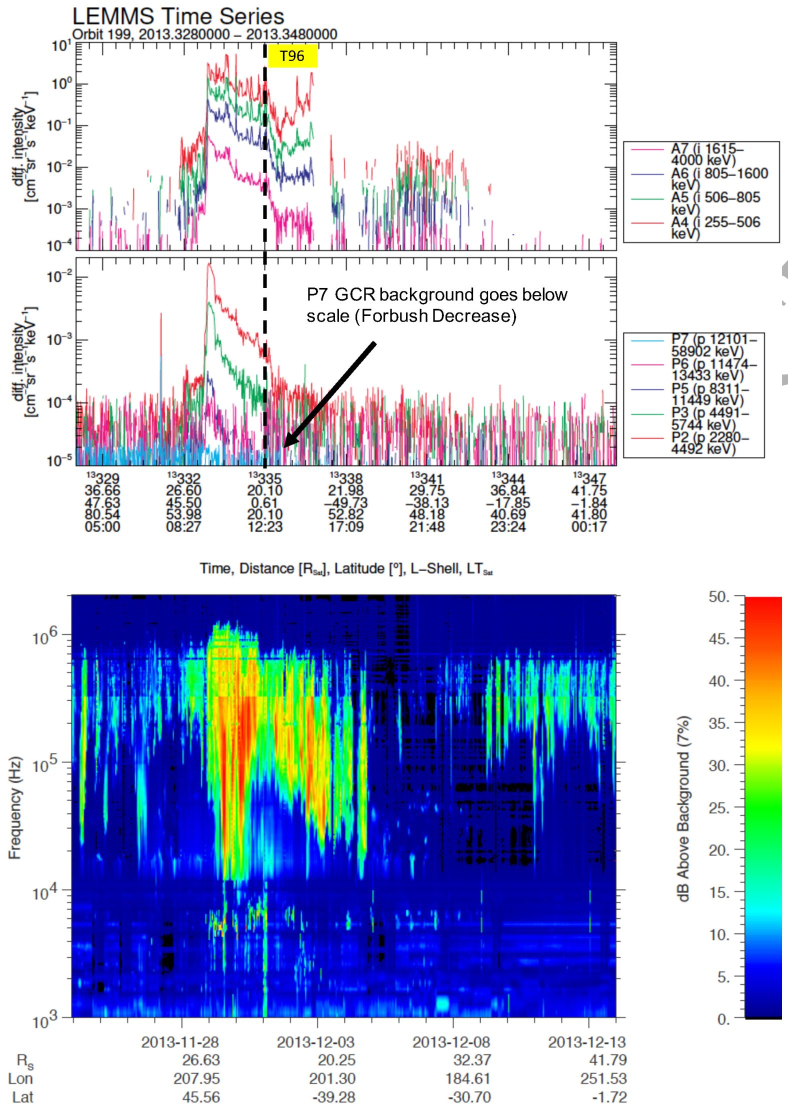

Figure 9: The two panels at the top show the profile of SEP event 31 in channels A4-A7 and P2-P7. Apparent gaps in several of the A-channel time-series are due to light contamination. Notice also how the GCR-driven background of channel P7 reduces below the range of the y-axis due to the associated FD. The bottom panel shows a frequency-time spectrogram from RPWS, with strong and persistent emissions of the Saturn Kilometric Radiation above 5 kHz coinciding with the SEP event. The time of Titan Flyby 96 (T96) is also marked.

ions appear already at the end of day 330. Enhanced LEMMS fluxes also coincide well with a period of strong Saturn Kilometric Radiation (SKR) emission that is extended to low frequencies (∼10 kHz), that have been associated to substorm-like events at Saturn or magnetospheric compressions (Taubenschuss et al., 2006; Jackman et al., 2010). The SKR enhancement persists for several rotations, hence, is more likely associated with a solar wind compression than a simple tail reconnection event. That is also supported by the observation of electron plasma oscillations at ∼5 kHz between days 333 and 336, indicating a solar wind plasma density of 0.3 cm^{-3}, with quiet solar wind values being typically between 0.05 and 0.1 cm^{-3} (Crary et al., 2005; Richardson and Burlaga, 2013).

Figure 10 shows the magnetic field components in KRTP coordinates and the magnetic field magnitude at the time of SEP event 31. Overplotted at the bottom panel is the average lobe field strength based on Jackman and Arridge (2011) (red line - Equation 1).

$$B_{lobe}[nT] = 251 \times r[R_S]^{-1.20} \tag{1}$$

At the beginning of the plotted interval Cassini is inside the magnetosphere, moving inbound. Following day 330 and until day 332, we observe consecutive dropouts magnitude coincident with increased fluctuations in the magnetic field indicative of magnetosheath encounters and transient compressions of the magnetosphere. Slightly before the SEP's peak (dotted-dashed line) a shock is visible as a sharp enhancement and rotation in the magnetic field. Sheath crossings continue until day 337, including occasional Cassini excursions into the solar wind, when also the single Titan flyby to date outside Saturn's bow-shock has taken place (Bertucci et al., 2015) (T96, day 335/2013). After day 337/2013, Cassini crosses the southern lobe of Saturn's magnetosphere where | B | remains significantly enhanced compared to B_{lobe} for about five days.

Clearly, the detection of event 31 guided the identification of a period of the enhanced solar wind conditions that the strong magnetospheric compression observed afterwards. The long-duration enhancement in the lobe magnetic field measured five days after the interplanetary shock and the compression induced by the high density solar wind seen with RPWS are highly relevant to magnetotail observations described by Jackman et al. (2010). The authors attributed similar measurements to the long-time scales required to fill Saturn's magnetotail with open flux before eventual compression and in-

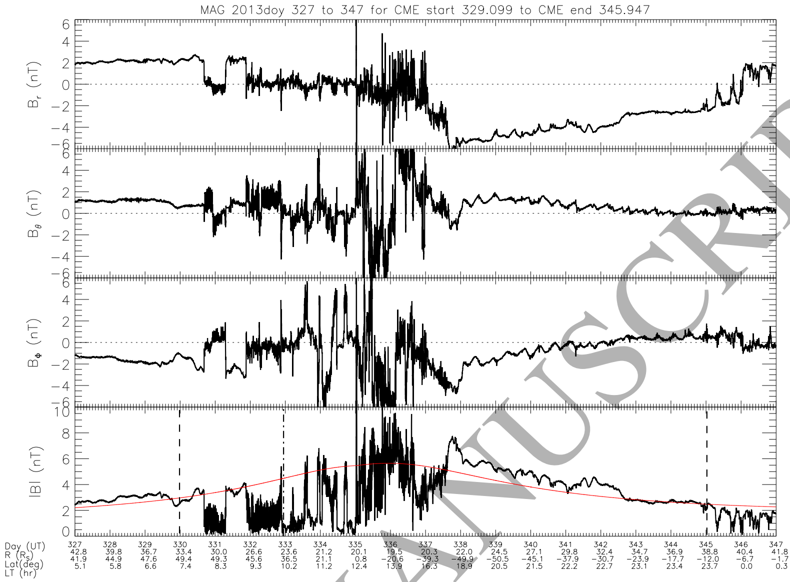

Figure 10: Magnetic field measurements around the time of SEP event 31. The field components are provided in the KRTP coordinate system. Dashed lines mark the start and end of the SEP event (based on LEMMS channel P2 measurements). The dotted-dashed line marks the time of the P2 peak count-rate. The red line at the bottom panel is is the average lobe field strength based on Jackman and Arridge (2011).

duced tail reconnection (Bunce et al., 2005; Thomsen et al., 2015), but relied on propagated solar wind properties (velocity, dynamic pressure) to derive the onset of the magnetospheric compression that were uncertain by 22 h. In our case, SEP 31 provides important context for timing the trigger process in the solar wind a higher accuracy. Additional observations of enhanced lobe fields may occur in connection with SEP events 13, 30, 32-34, 37, 38, 40 and 42-45, offer a considerable statistical sample for understanding open flux loading at Saturn and the associated time-scales.

7. Summary

In this study with surveyed the dataset of the MIMI/LEMMS energetic particle detector and used also inputs from MIMI/CHEMS, MAG and CAPS and RPWS to identify and characterize 46 SEP events and 17 intervals where a solar periodicity is seen in GCRs. The survey covered the period between 2004/160 and the end of 2015.

Given the absence of a solar wind monitor, SEPs and GCRs are valuable tracers of perturbed solar wind at Saturn. The main advantage of these particles, namely the possibility to continuously monitor them in and outside the magnetosphere, highlights an additional reason for including energetic ion and GCR monitoring systems (∼1 to several 100 MeV/n) for future missions that study the outer planets' magnetospheres.

Monitoring the upstream conditions through SEPs and GCRs is of course an indirect method as we cannot obtain any information about the interplanetary magnetic field and the plasma moments in the solar wind when the spacecraft is within Saturn's magnetosphere. The problem can be partly mitigated by using the peak SEP times and the onset of FDs as a guide to better constrain or identify the arrival times of interplanetary shocks or solar wind compressions with measurements from other Cassini instruments such as MAG, CAPS, RPWS.

SEP event peaks are usually within 4 days from the arrival of a shocks, while the onset of FDs can, under certain circumstances, refine this time to an accuracy of few hours. The results can be used for "calibrating" solar wind propagation models (Tao et al., 2005; Zieger and Hansen, 2008), that will in turn provide the time series of solar wind parameters. Interplanetary shocks may also be identified in the SEP profiles as short duration, spiky enhancements in intensity (Reames, 1999), in which case their crossing times can be accurate to less than an hour. Such a dedicated analysis for each of the 46 events (many of which are highly structured) was beyond the scope of this study. We should also stress that depending on the application, different aspects of an SEP may be relevant. For instance, for the study of Titan's low altitude atmospheric ionization by SEPs, what is important is the time that Titan is exposed to MeV ions and the properties of the energetic ion spectra, not just the accurate timing of an interplanetary shock.

We demonstrated the value of our survey results in three cases. In the first case, we have shown that a previously reported observation of a quasi-periodic, ∼14-20 day expansion of Saturn's electron radiation belts (Roussos

Application/Interesting intervals	SEP events Periodic GCR intervals	Notes
Solar wind or CME propagation model validation, outer heliosphere studies	All	Tao et al. (2005); Zieger and Hansen (2008)
Transient radiation belts	4, 9, 10, 24	Roussos et al. (2008), see also Section 6.1
Inner magnetospheric response (in situ)	10, 13, 18, 20, 21, 23, 26, 27, 29, 31, 34, 38, 40	For cases of SEP peaks very close to the time of the periapsis
Outer magnetosphere response (including tail, lobes, magnetopause)	All excluding 1, 4, 5, 6, 11, 14, 25, 36	Excluded intervals do not cross into the magnetosphere, but can provide upper limits for the magnetopause distance
Magnetospheric response (Energetic Neutral Atoms)	All	Condition of large distance (≥20 Rs) for global ENA imaging satisfied almost always as SEPs usually last over a week
Magnetospheric response (aurora)	13, 16, 18, 19, 24, 27, 29-35, 38, 39, 43-45	Based on the availability of UVIS/HST imaging of the aurora
Extended duration disturbance #1	3-11	End of 2004 to 2006 period with three very intense SEPs and several moderate ones
Extended duration disturbance #2	19-24	Abrupt changes in Planetary Period Oscillations and long-duration dropouts in radiation belts Provan et al. (2013); Roussos et al. (2014)
Extended duration disturbance #3	34-45	Nearly continuous SEP occurrence between days 240/2014 - 210/2015
Titan flybys during SEPs	3, 9 ,10, 13 15, 16, 20, 23, 26, 30-32, 34, 38, 40, 42, 45	Flybys: TC, T6, T7, T22, T37, T38, T39 T77, T81, T82, T85, T94, T96, T98, T105, T108, T109, T110, T112
Multi-instrument, upstream solar wind monitoring	All	Identify other indices of enhanced SW e.g. Low-Frequency-Extension of Saturn kilometric radiation (Jackman et al., 2010)
CIR compression/rarefaction times	All	Based on minima/maxima of periodic GCR intervals
Solar periodicities in the magnetosphere	All	Carbary et al. (2013); Carbary and Rymer (2017) Figure 6

Table 5: A list of potential applications based on the event catalogs given in Tables 1-4. In the middle column, red font refers to Table 4, the rest to Tables 1-3

et al., 2014), coincides with a time interval that a ∼13-day periodicity, typical for two CIRs per solar rotation, is seen in GCRs (Figure 6). That indicates the solar wind can exert a significant control in the structure and intensity of Saturn's electron radiation belts, despite the fact that they reside in a strong dipolar region of a giant, internally driven magnetosphere. It remains unclear, however, why such clear signatures are seen more frequently. It is very likely that this control becomes apparent only for the strongest perturbations induced by the solar wind. Alternatively, perturbations by other magnetospheric processes (e.g. tail reconnection/injections) that may also influence the electron belts, are frequently superimposed and mixed making difficult to decompose and assess the different contributions.

In another application (Section 6.1), we have shown that the formation of transient radiation belts at Saturn is a two-step process: MeV ions from an SEP event can easily penetrate across the magnetopause and populate the magnetosphere down to an L-shell of ∼8, after which the planet's magnetic field acts as a barrier to fast radial transport. Solar wind-induced magnetospheric convection, driven e.g. by an interplanetary shock that is associated to an SEP, may then enable the fast transport of MeV ions to lower L-shells and the formation of a transient ion belt. Convection may also lead to fast electron transport and to the appearance of the corresponding transient electron radiation belts, the observation of which on days 104-105/2012 is reported here for the first time.

Finally, in Section 6.2 we have shown that the impulsive SEP event 31 of day 332/2013 was the definite source of a strong magnetospheric compression and open flux loading in the magnetotail. The onset of this disturbance can now be identified and the time scales of flux loading can be better estimated. The same active period was responsible for the observation of Titan in the solar wind (flyby T96) (Bertucci et al., 2015), during which the moon's atmosphere should have been exposed to unusually high fluxes fluxes of MeV ions that can ionize its lower atmosphere at an enhanced rate.

Applications of our SEP list are, of course, not limited to the few examples analyzed here. We list some additional applications in Table 5. We will continue to survey the LEMMS data for more SEPs until the end of the Cassini mission (September 2017), develop our methodology for detecting SEP transients and update the event lists whenever new information becomes available.

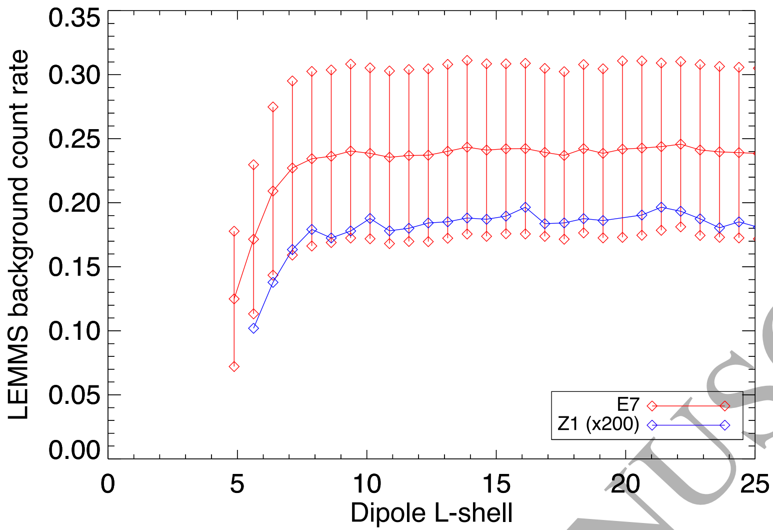

Figure A.11: The dipole L-shell profile of the GCR-driven background from two LEMMS MeV particle channels. Error bars are shown only for E7. They are similar for Z1, which has been shifted by a factor 200 for a better comparison of the two profiles.

Appendix A. GCR access in Saturn's magnetosphere

Figure A.11 shows the dipole L-shell profile of the background count-rate from two LEMMS channels: E7 (nominally $\gtrsim$7 MeV electrons) and Z1 (3.43 - 9.37 MeV/n for oxygen). These channels measure foreground only in the radiation belts and inside about L=4.5, a region excluded from this plot. For L>4.5 they are dominated by GCR background, apart from two short periods that Z1 measured oxygen during an SEP. The profile is representative of the GCR integral flux above several hundred MeV. The obscuration of the sky by Saturn and its rings, as well as the strong magnetic field of the planet start to gradually exclude GCRs from L$\sim$8-10. A similar behavior is seen in many other LEMMS channels with a GCR-driven instrumental background. In order to create this profile we used all channel measurements from Saturn Orbit Insertion to 2017. The error bars represent mostly the statistical scatter of the background rates and to a lesser extent the solar cycle modulation of the GCRs, which has not been removed, as it is much smaller than the scatter. Numerical GCR tracing results by Kotova (2016) are consistent with these observations.

Appendix B. Plots of SEP intervals

In this Appendix we show plots of the Table 1-3 SEPs. We display them with data from ion channels P2 and P3 on the top panel. The bottom panel tracks the GCR strength using the background measurements of electron channel E6. In all panels and plots, data were averaged in time bins of 6 hours while L<12 were excluded. Spikes in the count-rate profiles (due to various LEMMS instrumental issues) were removed using a median filtering. Since we did not find a unique threshold value for our median filter that removes all spikes without also removing valid data, there are few intervals with residual, spiky enhancements. All these were carefully inspected to avoid misidentifying them with an SEP (e.g. spikes in channel P2 on days 120-130/2005). Shaded areas mark the SEP intervals. Black vertical dashed lines indicate periapsis times, red lines the peak count rate in LEMMS channel P2 for each SEP interval. We create one plot per year, starting on day 200/2004. No plots are shown for years 2009 and 2010, when no SEPs were observed.

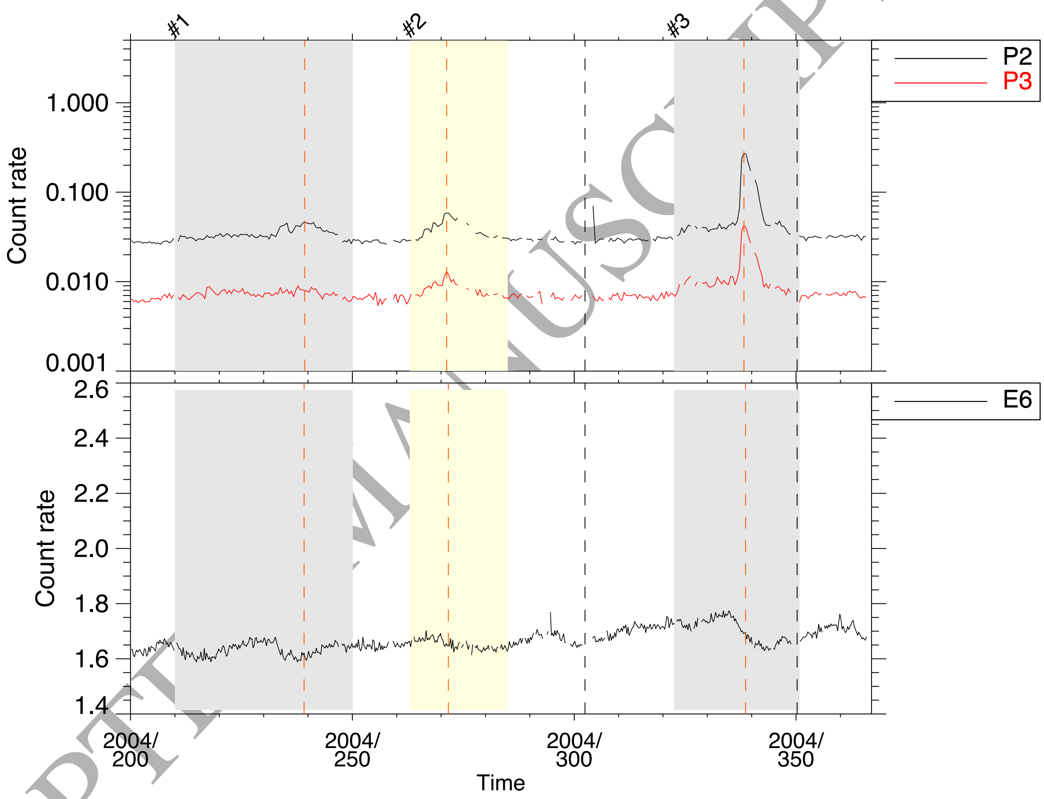

Figure B.12: SEP events in 2004. The top shows the count-rate of channels P2 and P3. P2 is the primary LEMMS channel used to identify SEPs. The bottom panel shows the GCR-driven count-rate of electron channel E6, where FDs can be observed. Shaded areas mark the SEP intervals. Black vertical dashed lines indicate periapsis times, red lines the peak count rate in LEMMS channel P2 for each SEP interval.

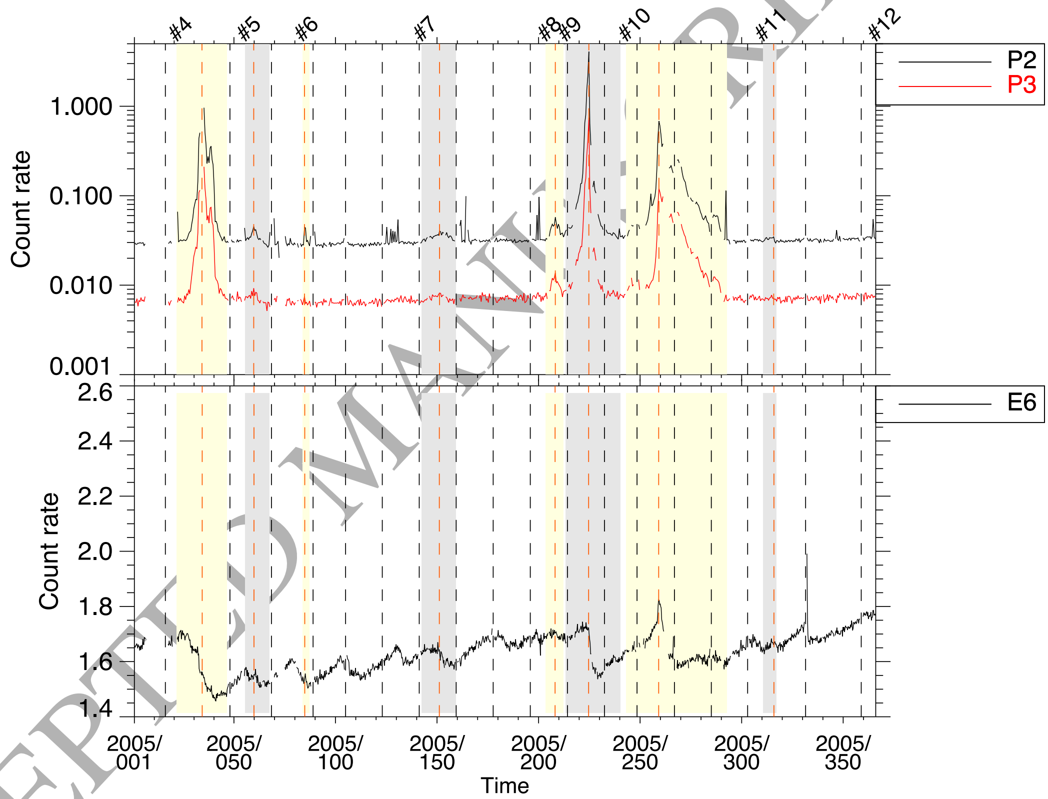

Figure B.13: Same as Figure B.12 for 2005.

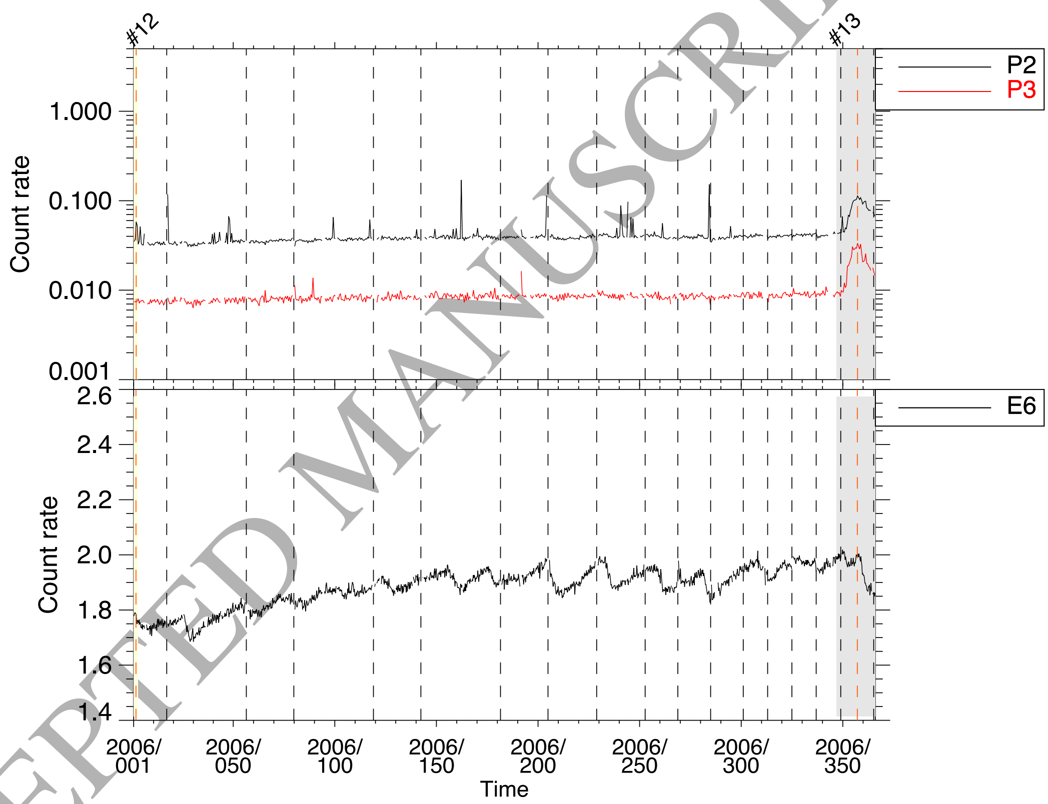

Figure B.14: Same as Figure B.12 for 2006.

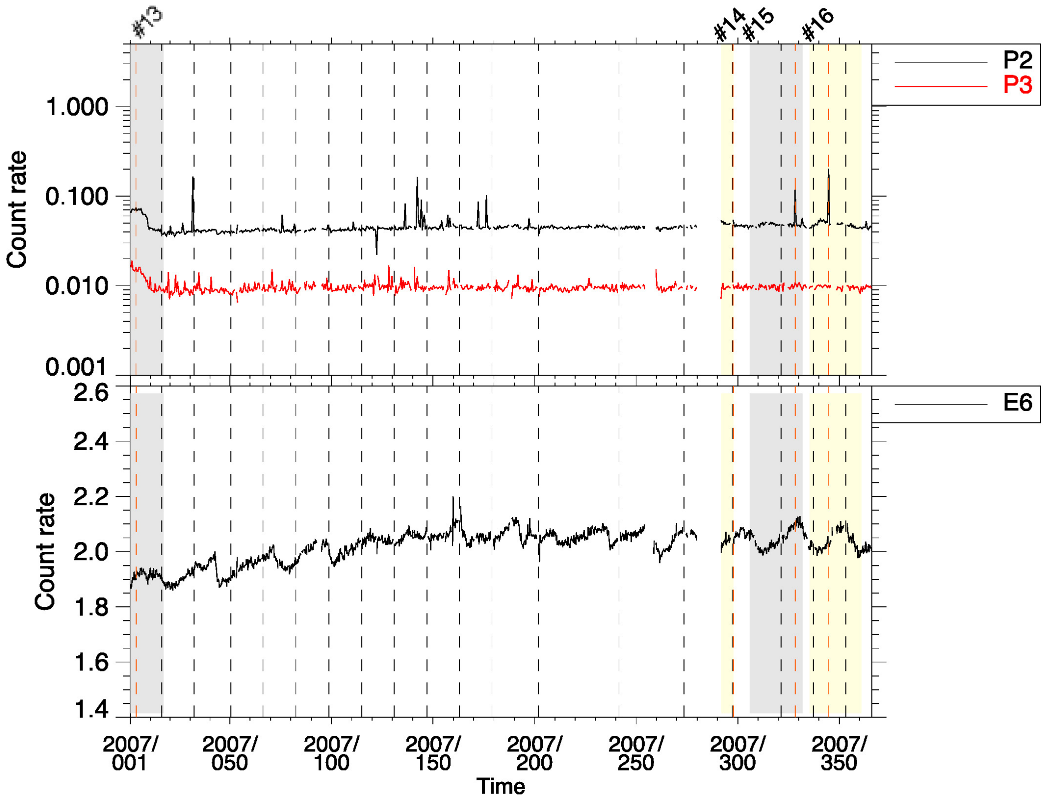

Figure B.15: Same as Figure B.12 for 2007.

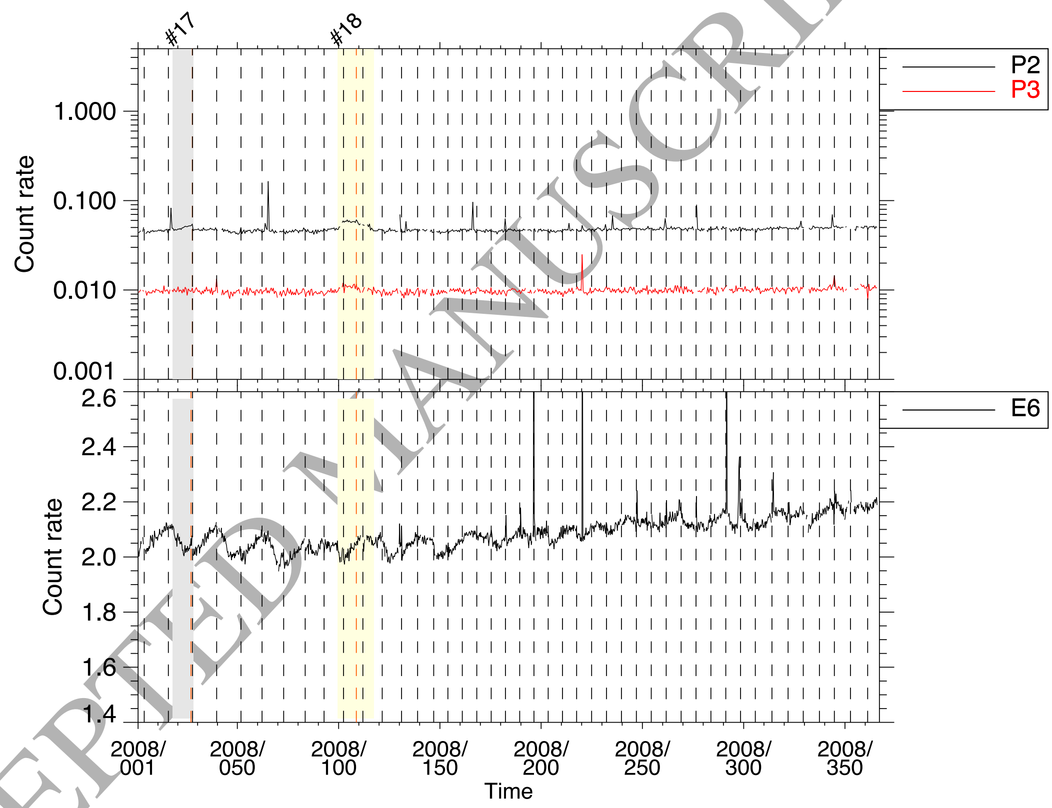

Figure B.16: Same as Figure B.12 for 2008.

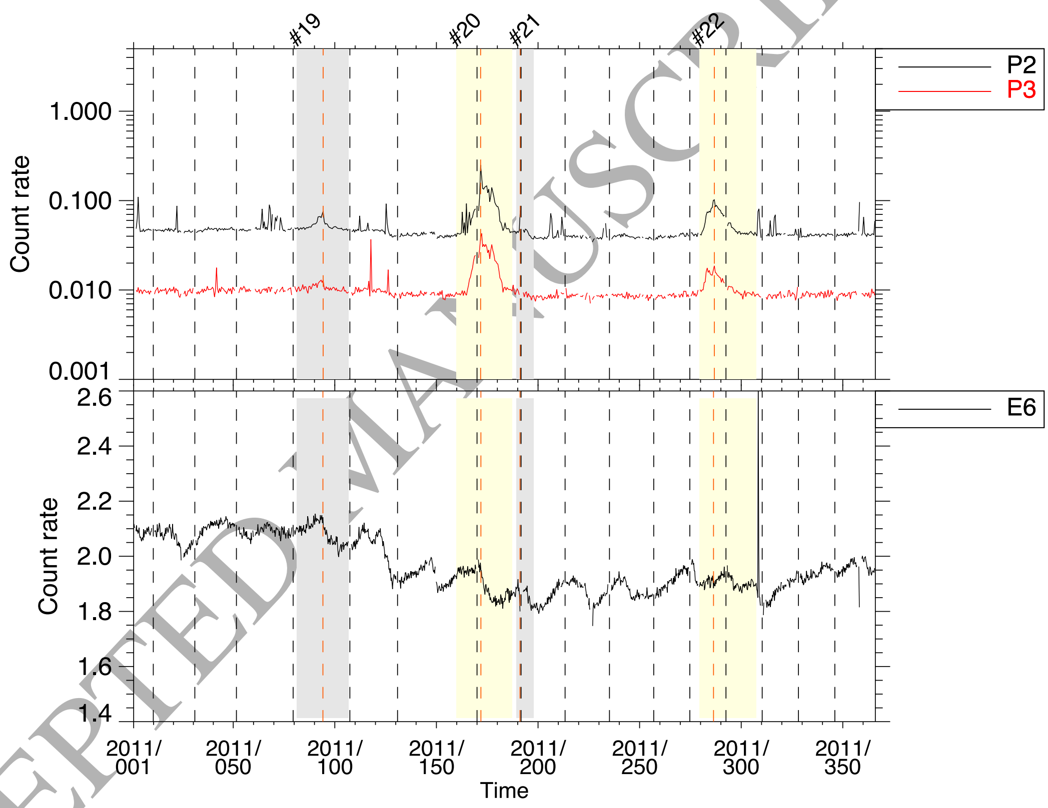

Figure B.17: Same as Figure B.12 for 2011.

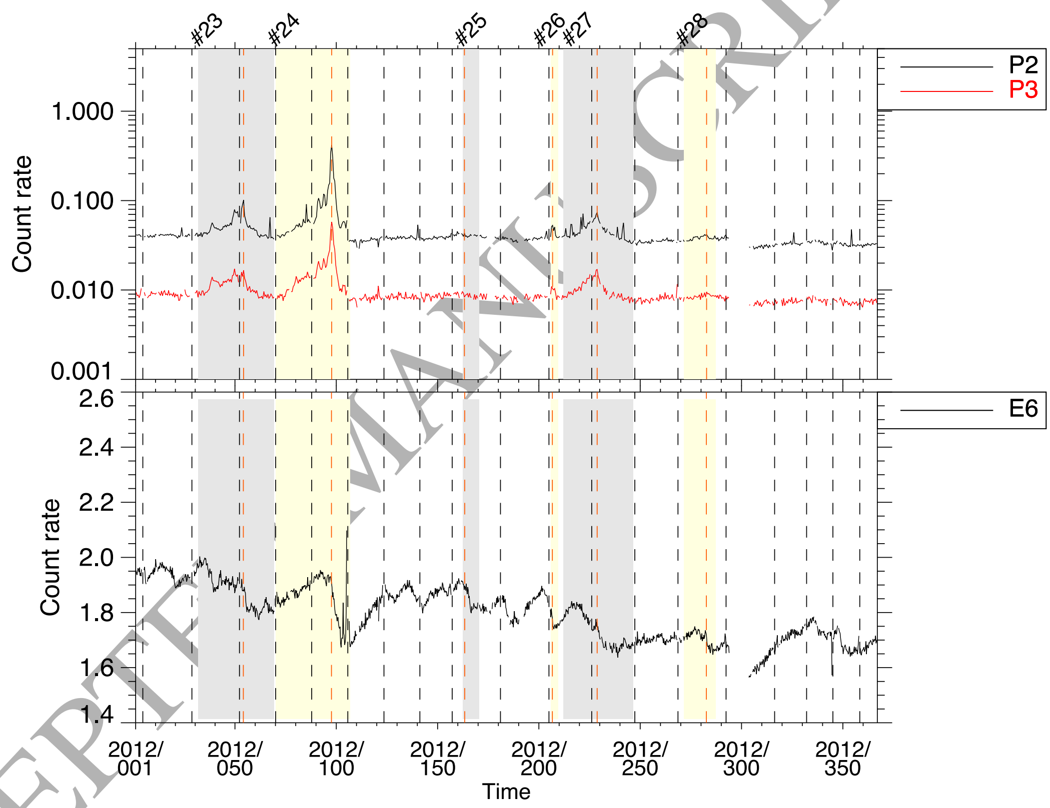

Figure B.18: Same as Figure B.12 for 2012.

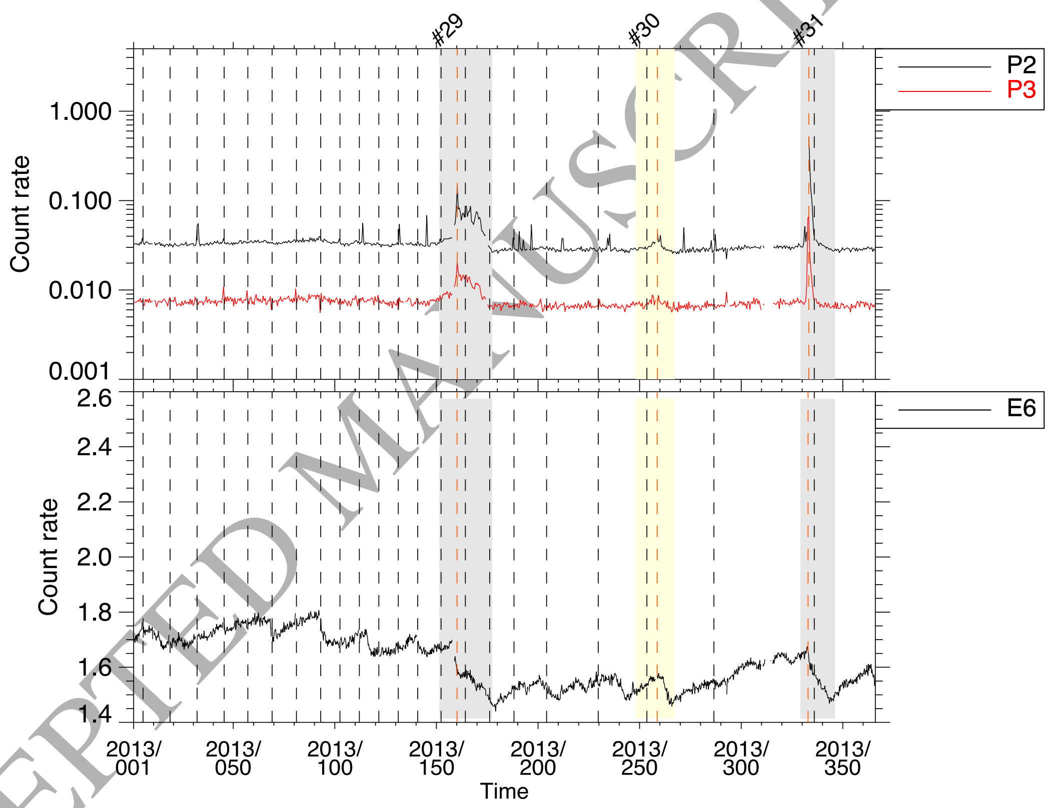

Figure B.19: Same as Figure B.12 for 2013.

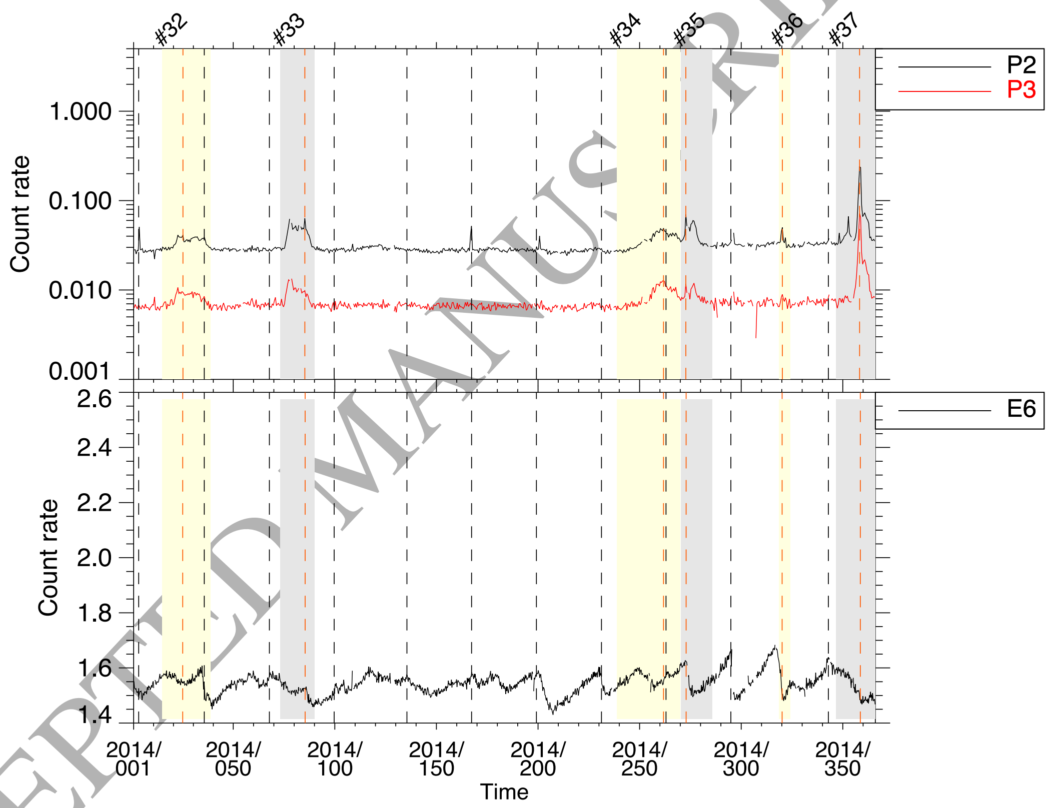

Figure B.20: Same as Figure B.12 for 2014.

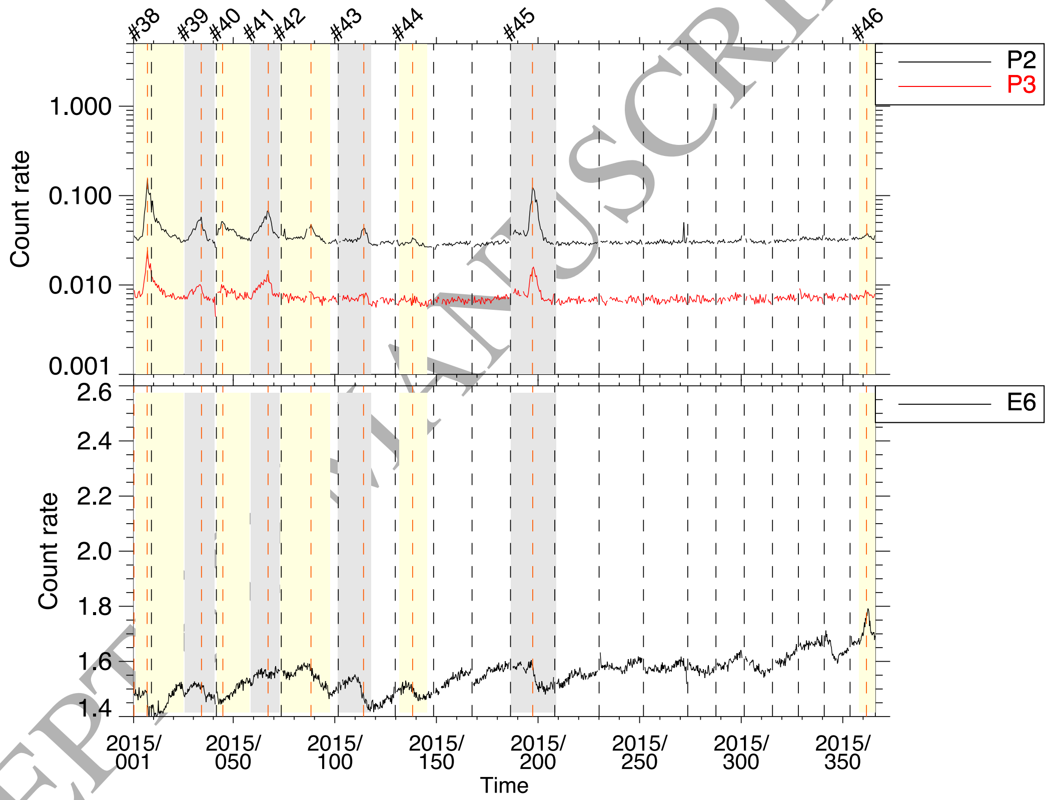

Figure B.21: Same as Figure B.12 for 2015.

Appendix C. LEMMS ion channels

Here we provide information about basic responses of MIMI/LEMMS ion channels used in our study. Table C.6 replicates information from Armstrong et al. (2009) and Krimigis et al. (2004) with some additional information in the "Notes" columns. For instance, it is stated that channel P1 has a strong response to ∼100 keV electrons which are abundant at all locations in Saturn's magnetosphere (Kollmann et al., 2011; Carbary et al., 2011; Roussos et al., 2016). This explains why P1 was not used here, even though its energy response to protons and similar geometry factor to P2 would have been ideal for the SEP survey. No information is given for the electron channels, as they are mainly used to indirectly measure GCRs.

Low Energy Telescope (LET)				High Energy Telescope (HET)			
Channel	Species	Energy [keV]	Notes	Channel	Species	Energy [MeV]	Notes
A0	Z≥1	27-35	Strong light contamination	P1	Z≥1	1.424-2.278	Strong response to ∼100 keV electrons
A1	Z≥1	35-56	Strong light contamination	P2	Z≥1	2.28-4.492	
A2	Z≥1	56-106	Light contamination at low Sun angles	P3	Z=1	4.491-5.744	
A3	Z≥1	106-255	Light contamination at low Sun angles	P4	Z=1	13.2-25.4	Lower energy response based on Krimigis et al. (2004)
A4	Z≥1	255-506	Light contamination at low Sun angles	P5	Z=1	8.311-11.45	
A5	Z≥1	506-805	Light contamination at low Sun angles	P6	Z=1	11.47-13.43	
A6	Z≥1	805-1600	Light contamination at low Sun angles	P7	Z=1,2	12.1-58.9	Weak MeV electron response
A7	Z≥1	1615-4000	Light contamination at low Sun angles	P8	Z=1, 2	25.19-59.0	
A8	Z≥2	1270-3930		P9	Z=1, 2	58.65-158.7	Strong MeV electron response
B0	Z=1	4000-7500	Spurious responses during light contamination	H1	Z≥2	2.1-4.4	
B1	Z=1	7500-18600		H2	Z≥2	4.4-10.3	
B2	Z=2, 8	3920-5470		H3	Z≥2	11-2-25.4	
B3	Z=2, 8	5470-9900		H4	Z=2	25.4-43.3	
				H5	Z=1, 2	20.0-25.0	
				Z1	Z≥8	3.43-9.37	
				Z2	Z≥8	9.37-24.7	
				Z3	Z≥8	24.7-193.0	

Table C.6: Basic information on LEMMS ion channels reviewed in this study. The information is primarily based on Armstrong et al. (2009) and Krimigis et al. (2004). "Z" in the "species" column corresponds to the atomic number. Energy ranges given are for the lowest Z number a channel responds to. Potential responses of some ion channels to H_2 or H_3 are not considered here.

Appendix D. Examples of two-step Forbush decreases in LEMMS data

Here we show three examples of two-step FDs in LEMMS data (Figure D.22). The plotted periods include few days of data from the FDs of events 3, 24 and 36 (Table 5), where LEMMS channel E6 is used as a GCR tracer. Data are averaged every 10^4 s, or 2.8 h. The two FD steps are marked in each case. We also use the example of event 24 (middle panel - also discussed in Section 6.1) to illustrate that radiation belt crossings are short compared to the duration of an FD, so filtering out those crossings (e.g. plots of Appendix B) has no impact in our assessment of SEP and GCR transients. Event 36 (bottom panel) is also analyzed in detail in Witasse et al. (2017).

Appendix E. Acknowledgments

We thank Andreas Lagg and Markus Fränz (MPS) for extensive software support, Martha Kusterer and Jon Vandegriff (both JHUAPL) for reducing the MIMI data. This work evolved from discussions held during a meetings of the International Space Science Institute teams on “Structure and Dynamics of Jupiter's magnetosphere and boundary regions” and “How does the Solar Wind Influence the Giant Planet Magnetospheres?”. Work at MPS was supported by the German Space Agency (DLR) through the contracts 50 OH 1101 and 50 OH 1502 and by the Max Planck Society. CMJ is supported by a Science and Technology Ernest Rutherford Fellowship number ST/L004399/1.Work at PSI was supported by the NASA Cassini program through JPL contract 1243218 with Southwest Research Institute. SVB was supported by STFC Fellowship ST/M005534/1. The work of RB is supported by the Deutsche Forschungsgemeinschaft under grant BU 3115/2-1.

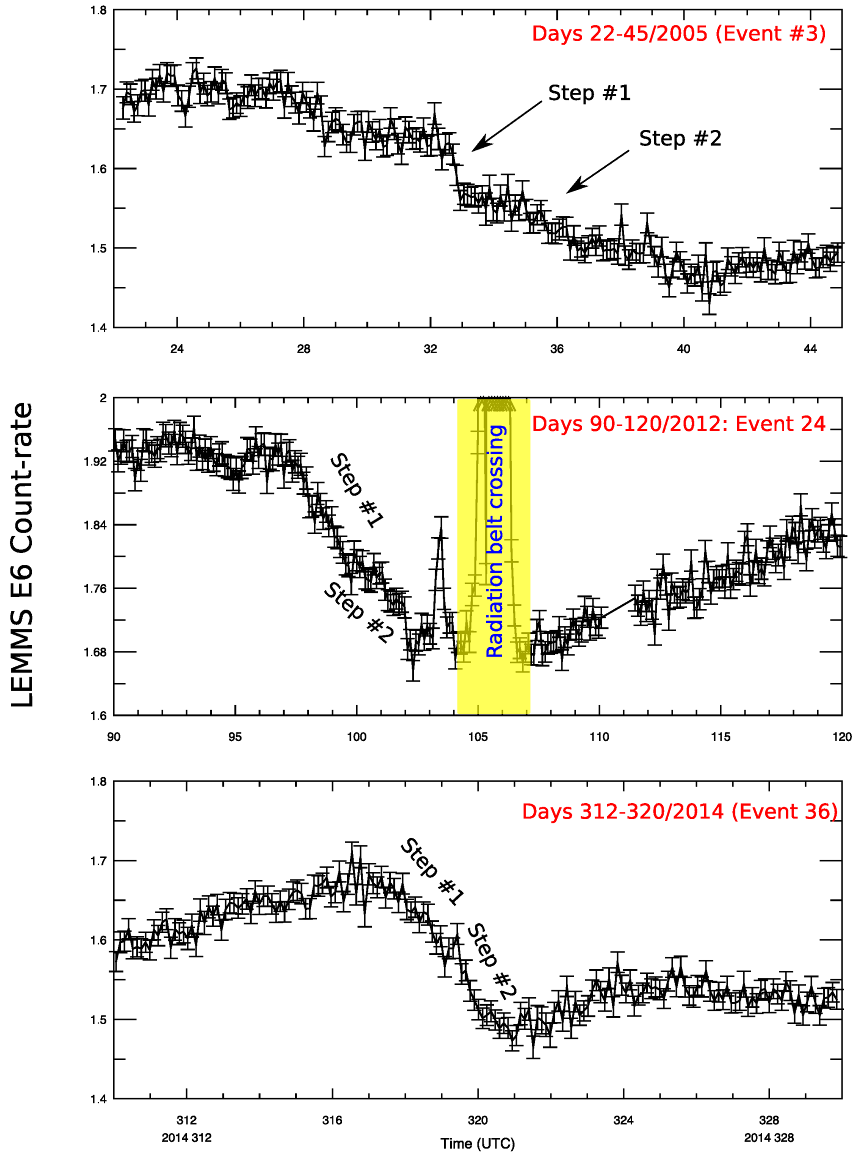

Figure D.22: Examples of two-step FDs in the LEMMS data.

References

Armstrong, T. P., Taherion, S., Manweiler, J., Krimigis, S., Paranicas, C., Mitchell, D., Krupp, N., Dec. 2009. Energetic ions trapped in Saturn's inner magnetosphere. Planetary and Space Science 57, 1723–1731.

Arunbabu, K. P., Antia, H. M., Dugad, S. R., Gupta, S. K., Hayashi, Y., Kawakami, S., Mohanty, P. K., Nonaka, T., Oshima, A., Subramanian, P., Jul. 2013. High-rigidity Forbush decreases: due to CMEs or shocks? A&A555, A139.

Barnes, C. W., Simpson, J. A., Dec. 1976. Evidence for interplanetary acceleration of nucleons in corotating interaction regions. ApJ210, L91–L96.

Bertucci, C., Hamilton, D. C., Kurth, W. S., Hospodarsky, G., Mitchell, D., Sergis, N., Edberg, N. J. T., Dougherty, M. K., 2015. Titan's interaction with the supersonic solar wind. Geophysical Research Letters 42 (2), 193–200, 2014GL062106.
URL http://dx.doi.org/10.1002/2014GL062106

Blanc, M., Andrews, D. J., Coates, A. J., Hamilton, D. C., Jackman, C. M., Jia, X., Kotova, A., Morooka, M., Smith, H. T., Westlake, J. H., Oct. 2015. Saturn Plasma Sources and Associated Transport Processes. Space Sci. Rev.192, 237–283.

Bunce, E. J., Cowley, S. W. H., Milan, S. E., 2005. Interplanetary magnetic field control of saturn's polar cusp aurora. Annales Geophysicae 23 (4), 1405–1431.
URL http://www.ann-geophys.net/23/1405/2005/

Burlaga, L. F., Ness, N. F., 1998. Voyager observations of the magnetic field in the distant heliosphere. Space Science Reviews 83 (1), 105–121.
URL http://dx.doi.org/10.1023/A:1005025613036

Bučík, R., Mall, U., Korth, A., Mason, G. M., Sep. 2009. On acceleration of <1 MeV/n He ions in the corotating compression regions near 1 AU: STEREO observations. Annales Geophysicae 27, 3677–3690.

Bučík, R., Mall, U., Korth, A., Mason, G. M., Jun. 2011. STEREO observations of the energetic ions in tilted corotating interaction regions. Journal of Geophysical Research (Space Physics) 116, A06103.

Cane, H. V., 2000. Coronal mass ejections and forbush decreases. Space Science Reviews 93 (1), 55–77.
URL http://dx.doi.org/10.1023/A:1026532125747

Cane, H. V., Reames, D. V., von Rosenvinge, T. T., 1988. The role of interplanetary shocks in the longitude distribution of solar energetic particles. Journal of Geophysical Research: Space Physics 93 (A9), 9555–9567.
URL http://dx.doi.org/10.1029/JA093iA09p09555

Carbary, J. F., Paranicas, C., Mitchell, D. G., Krimigis, S. M., Krupp, N., 2011. Energetic electron spectra in saturn's plasma sheet. Journal of Geophysical Research: Space Physics 116 (A7).
URL http://dx.doi.org/10.1029/2011JA016598

Carbary, J. F., Roelof, E. C., Mitchell, D. G., Hamilton, D. C., 2013. Solar periodicity in energetic ions at saturn. Journal of Geophysical Research: Space Physics 118 (5), 1891–1898.
URL http://dx.doi.org/10.1002/jgra.50282

Carbary, J. F., Rymer, A. M., 2017. Solar wind periodicities in thermal electrons at saturn. Journal of Geophysical Research: Space Physics 122 (1), 150–155, 2016JA023531.
URL http://dx.doi.org/10.1002/2016JA023531

Carbary, J. F., Sergis, N., Mitchell, D. G., Krupp, N., 2015. Saturn's hinge parameter from cassini magnetotail passes in 20132014. Journal of Geophysical Research: Space Physics 120 (6), 4438–4445, 2015JA021152.
URL http://dx.doi.org/10.1002/2015JA021152

Crary, F. J., Clarke, J. T., Dougherty, M. K., Hanlon, P. G., Hansen, K. C., Steinberg, J. T., Barraclough, B. L., Coates, A. J., Gérard, J.-C., Grodent, D., Kurth, W. S., Mitchell, D. G., Rymer, A. M., Young, D. T., Feb. 2005. Solar wind dynamic pressure and electric field as the main factors controlling Saturn's aurorae. Nature433, 720–722.

Delamere, P. A., Bagenal, F., Paranicas, C., Masters, A., Radioti, A., Bonfond, B., Ray, L., Jia, X., Nichols, J., Arridge, C., Apr. 2015. Solar Wind and Internally Driven Dynamics: Influences on Magnetodiscs and Auroral Responses. Space Sci. Rev.187, 51–97.

Desai, M. I., Mason, G. M., Gold, R. E., Krimigis, S. M., Cohen, C. M. S., Mewaldt, R. A., Mazur, J. E., Dwyer, J. R., Sep. 2006. Heavy-Ion Elemental Abundances in Large Solar Energetic Particle Events and Their Implications for the Seed Population. ApJ649, 470–489.

Dialynas, K., Krimigis, S. M., Mitchell, D. G., Hamilton, D. C., Krupp, N., Brandt, P. C., Jan. 2009. Energetic ion spectral characteristics in the Saturnian magnetosphere using Cassini/MIMI measurements. Journal of Geophysical Research (Space Physics) 114, 1212.

Dougherty, M. K., Kellock, S., Southwood, D. J., Balogh, A., Smith, E. J., Tsurutani, B. T., Gerlach, B., Glassmeier, K., Gleim, F., Russell, C. T., Erdos, G., Neubauer, F. M., Cowley, S. W. H., Sep. 2004. The Cassini Magnetic Field Investigation. Space Science Reviews 114, 331–383.

Dougherty, M. K., Khurana, K. K., Neubauer, F. M., Russell, C. T., Saur, J., Leisner, J. S., Burton, M. E., Mar. 2006. Identification of a Dynamic Atmosphere at Enceladus with the Cassini Magnetometer. Science 311, 1406–1409.

Foullon, C., Owen, C. J., Dasso, S., Green, L. M., Dandouras, I., Elliott, H. A., Fazakerley, A. N., Bogdanova, Y. V., Crooker, N. U., Aug. 2007. Multi-Spacecraft Study of the 21 January 2005 ICME. Evidence of Current Sheet Substructure Near the Periphery of a Strongly Expanding, Fast Magnetic Cloud. Solar Physics 244, 139–165.

Gosling, J., Pizzo, V., 1999. Formation and evolution of corotating interaction regions and their three dimensional structure. Space Science Reviews 89 (1), 21–52.
URL http://dx.doi.org/10.1023/A:1005291711900

Gurnett, D. A., Kurth, W. S., Kirchner, D. L., Hospodarsky, G. B., Averkamp, T. F., Zarka, P., Lecacheux, A., Manning, R., Roux, A., Canu, P., Cornilleau-Wehrlin, N., Galopeau, P., Meyer, A., Boström, R., Gustafsson, G., Wahlund, J., Åhlen, L., Rucker, H. O., Ladreiter, H. P., Macher, W., Woolliscroft, L. J. C., Alleyne, H., Kaiser, M. L., Desch, M. D., Farrell, W. M., Harvey, C. C., Louarn, P., Kellogg, P. J., Goetz, K., Pedersen, A., Sep. 2004. The Cassini Radio and Plasma Wave Investigation. Space Science Reviews 114, 395–463.

Hudson, M. K., Elkington, S. R., Lyon, J. G., Marchenko, V. A., Roth, I., Temerin, M., Blake, J. B., Gussenhoven, M. S., Wygant, J. R., 1997. Simulations of radiation belt formation during storm sudden commencements. Journal of Geophysical Research: Space Physics 102 (A7), 14087–14102. URL http://dx.doi.org/10.1029/97JA03995

Hudson, M. K., Kotelnikov, A. D., Li, X., Roth, I., Temerin, M., Wygant, J., Blake, J. B., Gussenhoven, M. S., 1995. Simulation of proton radiation belt formation during the march 24, 1991 ssc. Geophysical Research Letters 22 (3), 291–294. URL http://dx.doi.org/10.1029/95GL00009

Jackman, C. M., Achilleos, N., Bunce, E. J., Cecconi, B., Clarke, J. T., Cowley, S. W. H., Kurth, W. S., Zarka, P., 2005. Interplanetary conditions and magnetospheric dynamics during the cassini orbit insertion fly-through of saturn's magnetosphere. Journal of Geophysical Research: Space Physics 110 (A10), a10212. URL http://dx.doi.org/10.1029/2005JA011054

Jackman, C. M., Achilleos, N., Bunce, E. J., Cowley, S. W. H., Dougherty, M. K., Jones, G. H., Milan, S. E., Smith, E. J., 2004. Interplanetary magnetic field at 9 au during the declining phase of the solar cycle and its implications for saturn's magnetospheric dynamics. Journal of Geophysical Research: Space Physics 109 (A11), a11203. URL http://dx.doi.org/10.1029/2004JA010614

Jackman, C. M., Arridge, C. S., May 2011. Statistical properties of the magnetic field in the Kronian magnetotail lobes and current sheet. Journal of Geophysical Research (Space Physics) 116, A05224.

Jackman, C. M., Arridge, C. S., Slavin, J. A., Milan, S. E., Lamy, L., Dougherty, M. K., Coates, A. J., 2010. In situ observations of the effect of a solar wind compression on saturn's magnetotail. Journal of Geophysical Research: Space Physics 115 (A10), a10240. URL http://dx.doi.org/10.1029/2010JA015312

Jackman, C. M., Forsyth, R. J., Dougherty, M. K., 2008. The overall configuration of the interplanetary magnetic field upstream of saturn as revealed by cassini observations. Journal of Geophysical Research: Space Physics

113 (A8), a08114.
URL http://dx.doi.org/10.1029/2008JA013083

Kollmann, P., Roussos, E., Paranicas, C., Krupp, N., Haggerty, D. K., Jan. 2013. Processes forming and sustaining Saturn's proton radiation belts. Icarus 222, 323–341.

Kollmann, P., Roussos, E., Paranicas, C., Krupp, N., Jackman, C. M., Kirsch, E., Glassmeier, K.-H., May 2011. Energetic particle phase space densities at Saturn: Cassini observations and interpretations. Journal of Geophysical Research (Space Physics) 116, A05222.

Kotova, A., Sep. 2016. Energetic particle tracking techniques and its application to the magnetosphere of Saturn. Theses, UNIVERSITE TOULOUSE III – PAUL SABATIER.
URL https://tel.archives-ouvertes.fr/tel-01401253

Krimigis, S. M., Mitchell, D. G., Hamilton, D. C., Livi, S., Dandouras, J., Jaskulek, S., Armstrong, T. P., Boldt, J. D., Cheng, A. F., Gloeckler, G., Hayes, J. R., Hsieh, K. C., Ip, W.-H., Keath, E. P., Kirsch, E., Krupp, N., Lanzerotti, L. J., Lundgren, R., Mauk, B. H., McEntire, R. W., Roelof, E. C., Schlemm, C. E., Tossman, B. E., Wilken, B., Williams, D. J., Sep. 2004. Magnetosphere Imaging Instrument (MIMI) on the Cassini Mission to Saturn/Titan. Space Science Reviews 114, 233–329.

Lario, D., Livi, S., Roelof, E. C., Decker, R. B., Krimigis, S. M., Dougherty, M. K., Sep. 2004. Heliospheric energetic particle observations by the Cassini spacecraft: Correlation with 1 AU observations. Journal of Geophysical Research (Space Physics) 109, A09S02.

Lario, D., Roelof, E. C., Decker, R. B., Ho, G. C., Maclennan, C. G., Gosling, J. T., 2003. Solar cycle variations of the energetic h/he intensity ratio at high heliolatitudes and in the ecliptic plane. Annales Geophysicae 21 (6), 1229–1243.
URL http://www.ann-geophys.net/21/1229/2003/

Lockwood, J. A., 1971. Forbush decreases in the cosmic radiation. Space Science Reviews 12 (5), 658–715.
URL http://dx.doi.org/10.1007/BF00173346

Meredith, C. J., Alexeev, I. I., Badman, S. V., Belenkaya, E. S., Cowley, S. W. H., Dougherty, M. K., Kalegaev, V. V., Lewis, G. R., Nichols, J. D., 2014. Saturn's dayside ultraviolet auroras: Evidence for morphological dependence on the direction of the upstream interplanetary magnetic field. Journal of Geophysical Research: Space Physics 119 (3), 1994–2008, 2013JA019598.
URL http://dx.doi.org/10.1002/2013JA019598

Miyoshi, Y., Kataoka, R., 2008. Flux enhancement of the outer radiation belt electrons after the arrival of stream interaction regions. Journal of Geophysical Research: Space Physics 113 (A3), n/a–n/a, a03S09.
URL http://dx.doi.org/10.1029/2007JA012506

Paranicas, C., Mitchell, D. G., Krimigis, S. M., Hamilton, D. C., Roussos, E., Krupp, N., Jones, G. H., Johnson, R. E., Cooper, J. F., Armstrong, T. P., Oct. 2008. Sources and losses of energetic protons in Saturn's magnetosphere. Icarus 197, 519–525.

Pilkington, N. M., Achilleos, N., Arridge, C. S., Guio, P., Masters, A., Ray, L. C., Sergis, N., Thomsen, M. F., Coates, A. J., Dougherty, M. K., 2015. Internally driven large-scale changes in the size of saturn's magnetosphere. Journal of Geophysical Research: Space Physics 120 (9), 7289–7306, 2015JA021290.
URL http://dx.doi.org/10.1002/2015JA021290

Prangé, R., Pallier, L., Hansen, K. C., Howard, R., Vourlidas, A., Courtin, R., Parkinson, C., Nov. 2004. An interplanetary shock traced by planetary auroral storms from the Sun to Saturn. Nature432, 78–81.

Prise, A. J., Harra, L. K., Matthews, S. A., Arridge, C. S., Achilleos, N., 2015. Analysis of a coronal mass ejection and corotating interaction region as they travel from the sun passing venus, earth, mars, and saturn. Journal of Geophysical Research: Space Physics 120 (3), 1566–1588, 2014JA020256.
URL http://dx.doi.org/10.1002/2014JA020256

Provan, G., Cowley, S. W. H., Sandhu, J., Andrews, D. J., Dougherty, M. K., Jun. 2013. Planetary period magnetic field oscillations in Saturn's magnetosphere: Postequinox abrupt nonmonotonic transitions to northern system dominance. Journal of Geophysical Research (Space Physics) 118, 3243–3264.

Provan, G., Tao, C., Cowley, S. W. H., Dougherty, M. K., Coates, A. J., 2015. Planetary period oscillations in saturn's magnetosphere: Examining the relationship between abrupt changes in behavior and solar wind-induced magnetospheric compressions and expansions. Journal of Geophysical Research: Space Physics 120 (11), 9524–9544, 2015JA021642.
URL http://dx.doi.org/10.1002/2015JA021642

Reames, D. V., 1999. Particle acceleration at the sun and in the heliosphere. Space Science Reviews 90 (3), 413–491.
URL http://dx.doi.org/10.1023/A:1005105831781

Richardson, J. D., Burlaga, L. F., Jun. 2013. The Solar Wind in the Outer Heliosphere and Heliosheath. Space Sci. Rev.176, 217–235.

Roussos, E., Krupp, N., Armstrong, T. P., Paranicas, C., Mitchell, D. G., Krimigis, S. M., Jones, G. H., Dialynas, K., Sergis, N., Hamilton, D. C., Nov. 2008. Discovery of a transient radiation belt at Saturn. Geophys. Res. Lett. 35, 22106.

Roussos, E., Krupp, N., Mitchell, D. G., Paranicas, C., Krimigis, S. M., Andriopoulou, M., Palmaerts, B., Kurth, W. S., Badman, S. V., Masters, A., Dougherty, M. K., Jan. 2016. Quasi-periodic injections of relativistic electrons in Saturn's outer magnetosphere. Icarus263, 101–116.

Roussos, E., Krupp, N., Paranicas, C., Carbary, J. F., Kollmann, P., Krimigis, S. M., Mitchell, D. G., Dec. 2014. The variable extension of Saturn's electron radiation belts. Planetary Space Sci. 104, 3–17.

Roussos, E., Krupp, N., Paranicas, C. P., Kollmann, P., Mitchell, D. G., Krimigis, S. M., Armstrong, T. P., Went, D. R., Dougherty, M. K., Jones, G. H., Feb. 2011. Long- and short-term variability of Saturn's ionic radiation belts. Journal of Geophysical Research (Space Physics) 116, A02217.

Sarris, T. E., Li, X., Tsaggas, N., Paschalidis, N., 2002. Modeling energetic particle injections in dynamic pulse fields with varying propagation speeds. Journal of Geophysical Research: Space Physics 107 (A3), SMP 1–1–SMP 1–10.
URL http://dx.doi.org/10.1029/2001JA900166

Selesnick, R. S., 2002. Cosmic ray access to jupiter's magnetosphere. Geophysical Research Letters 29 (9), 12–1–12–4.
URL http://dx.doi.org/10.1029/2001GL014146

Simon, S., Saur, J., Neubauer, F. M., Wennmacher, A., Dougherty, M. K., Aug. 2011. Magnetic signatures of a tenuous atmosphere at Dione. Geophys. Res. Lett. 38, 15102.

Simpson, J., 1998. Recurrent solar modulation of the galactic cosmic rays and the anomalous nuclear component in three dimensions of the heliosphere. Space Science Reviews 83 (1), 7–19.
URL http://dx.doi.org/10.1023/A:1005055505768

Tao, C., Kataoka, R., Fukunishi, H., Takahashi, Y., Yokoyama, T., 2005. Magnetic field variations in the jovian magnetotail induced by solar wind dynamic pressure enhancements. Journal of Geophysical Research: Space Physics 110 (A11), a11208.
URL http://dx.doi.org/10.1029/2004JA010959

Taubenschuss, U., Rucker, H. O., Kurth, W. S., Cecconi, B., Zarka, P., Dougherty, M. K., Steinberg, J. T., Nov. 2006. Linear prediction studies for the solar wind and Saturn kilometric radiation. Annales Geophysicae 24 (11), 3139–3150.
URL https://hal.archives-ouvertes.fr/hal-00330098

Teolis, B., Waite, J., 2016. Dione and rhea seasonal exospheres revealed by cassini {CAPS} and {INMS}. Icarus 272, 277 – 289.
URL http://www.sciencedirect.com/science/article/pii/S0019103516001093

Thomsen, M. F., Jackman, C. M., Mitchell, D. G., Hospodarsky, G., Kurth, W. S., Hansen, K. C., Dec. 2015. Sustained lobe reconnection in Saturn's magnetotail. Journal of Geophysical Research (Space Physics) 120, 10.

Wang, C., Richardson, J. D., 2002. Development of a strong shock in the outer heliosphere. Geophysical Research Letters 29 (8), 22–1–22–4.
URL http://dx.doi.org/10.1029/2001GL014472

Wang, Y.-M., N. R. Sheeley, J., 2015. Coronal mass ejections and the solar cycle variation of the sun's open flux. The Astrophysical Journal Letters

809 (2), L24.
URL http://stacks.iop.org/2041-8205/809/i=2/a=L24

Webb, D. F., Howard, R. A., 1994. The solar cycle variation of coronal mass ejections and the solar wind mass flux. Journal of Geophysical Research: Space Physics 99 (A3), 4201–4220.
URL http://dx.doi.org/10.1029/93JA02742

Witasse, O., Snchez-Cano, B., Mays, M. L., Kajdi, P., Opgenoorth, H., Elliott, H. A., Richardson, I. G., Zouganelis, I., Zender, J., Wimmer-Schweingruber, R. F., Turc, L., Taylor, M. G. G. T., Roussos, E., Rouillard, A., Richter, I., Richardson, J. D., Ramstad, R., Provan, G., Posner, A., Plaut, J. J., Odstrcil, D., Nilsson, H., Niemenen, P., Milan, S. E., Mandt, K., Lohf, H., Lester, M., Lebreton, J.-P., Kuulkers, E., Krupp, N., Koenders, C., James, M. K., Intzekara, D., Holmstrom, M., Hassler, D. M., Hall, B. E. S., Guo, J., Goldstein, R., Goetz, C., Glassmeier, K. H., Gnot, V., Evans, H., Espley, J., Edberg, N. J. T., Dougherty, M., Cowley, S. W. H., Burch, J., Behar, E., Barabash, S., Andrews, D. J., Altobelli, N., 2017. Interplanetary coronal mass ejection observed at stereo-a, mars, comet 67p/churyumov-gerasimenko, saturn, and new horizons en-route to pluto. comparison of its forbush decreases at 1.4, 3.1 and 9.9 au. Journal of Geophysical Research: Space Physics, n/a–n/a2017JA023884.
URL http://dx.doi.org/10.1002/2017JA023884

Young, D. T., Berthelier, J. J., Blanc, M., Burch, J. L., Coates, A. J., Goldstein, R., Grande, M., Hill, T. W., Johnson, R. E., Kelha, V., McComas, D. J., Sittler, E. C., Svenes, K. R., Szegö, K., Tanskanen, P., Ahola, K., Anderson, D., Bakshi, S., Baragiola, R. A., Barraclough, B. L., Black, R. K., Bolton, S., Booker, T., Bowman, R., Casey, P., Crary, F. J., Delapp, D., Dirks, G., Eaker, N., Funsten, H., Furman, J. D., Gosling, J. T., Hannula, H., Holmlund, C., Huomo, H., Illiano, J. M., Jensen, P., Johnson, M. A., Linder, D. R., Luntama, T., Maurice, S., McCabe, K. P., Mursula, K., Narheim, B. T., Nordholt, J. E., Preece, A., Rudzki, J., Ruitberg, A., Smith, K., Szalai, S., Thomsen, M. F., Viherkanto, K., Vilppola, J., Vollmer, T., Wahl, T. E., Wüest, M., Ylikorpi, T., Zinsmeyer, C., Sep. 2004. Cassini Plasma Spectrometer Investigation. Space Science Reviews 114, 1–4.

Zhang, Y., Sun, W., Feng, X. S., Deehr, C. S., Fry, C. D., Dryer, M., 2008.

Statistical analysis of corotating interaction regions and their geoeffectiveness during solar cycle 23. Journal of Geophysical Research: Space Physics 113 (A8), a08106.
URL http://dx.doi.org/10.1029/2008JA013095

Zieger, B., Hansen, K. C., Aug. 2008. Statistical validation of a solar wind propagation model from 1 to 10 AU. Journal of Geophysical Research (Space Physics) 113, 8107.